IEEE Open Journal of the
Industrial Electronics Society

Received 26 February 2022; revised 17 March 2022; accepted 22 March 2022. Date of publication 25 March 2022;
date of current version 12 May 2022. The review of this paper was arranged by Associate Editor Haitham Abu-Rub.

Digital Object Identifier 10.1109/OJIES.2022.3162336

Analytical Prototype Functions for Flux Linkage Approximation in Synchronous Machines

SHIH-WEI SU [1], CHRISTOPH M. HACKL [2] (Senior Member, IEEE), AND RALPH KENNEL [1] (Senior Member, IEEE)

[1] Institute of Electrical Drive System and Power Electronics, Technical University of Munich, 80333 Munich, Germany
[2] Department of Electrical Engineering and Information Technology, Hochschule München University of Applied Sciences, 80335 Munich, Germany

CORRESPONDING AUTHOR: SHIH-WEI SU (e-mail: shihwei.su@tum.de).

ABSTRACT Physically motivated and analytical prototype functions are proposed to approximate the nonlinear flux linkages of nonlinear synchronous machines (SMs) in general; and reluctance synchronous machines (RSMs) and interior permanent magnet synchronous machines (IPMSMs) in particular. Such analytical functions obviate the need of huge lookup tables (LUTs) and are beneficial for optimal operation management and nonlinear control of such machines. The proposed flux linkage prototype functions are capable of mimicking the nonlinear self-axis and cross-coupling saturation effects of SMs. Moreover, the differentiable prototype functions allow to easily derive analytical expressions for the differential inductances by simple differentiation of the analytical flux linkage prototype functions. In total, two types of flux linkage prototype functions are developed. The first flux linkage approximation is rather simple and obeys the energy conservation rule for "symmetric" flux linkages of RSMs. With the gained knowledge, the second type of prototype functions is derived in order to achieve approximation flexibility necessary for SMs with permanent (or electrical) excitation with "unsymmetric" flux linkages due to the excitation offset. All proposed flux linkage prototype functions are continuously differentiable, obey the energy conservation rule and, as fitting results show, achieve a (very) high approximation accuracy over the whole operation range.

INDEX TERMS Analytical flux linkage prototype functions, interior permanent magnet synchronous machine, reluctance synchronous machine, saturation effects.

I. INTRODUCTION

With the developed manufacturing and control techniques and the increased efficiency requirements, induction machines (IMs) are more and more replaced by synchronous machines (SMs) [1]. Reluctance synchronous machines (RSMs) and permanent magnet synchronous machines (PMSMs) achieve higher efficiencies and better overall performance.

Except surface-mounted PMSM (SPMSM), both RSM and interior PMSM (IPMSM) exhibit significant magnetic saturation [2], [3], resulting in highly nonlinear flux linkages which depend on not only the direct-axis current but also the quadrature-axis current, leading to magnetic cross-coupling. In order to achieve the best possible drive performance, the saturation and cross-coupling effects cannot be neglected. The effectiveness of developed control algorithms, e.g., nonlinear current control strategies [4], optimal feedforward torque control (OFTC) [5], [6] or model predictive control [7], is deteriorated by model and parameter uncertainties. In addition, cross-coupling inductances [8] lead to position estimation errors in encoderless control. Consequently, a comprehensive flux linkage (or differential inductance) model is essential for the control of modern electrical drive systems.

The magnetic nonlinearity of the flux linkage maps can normally be extracted (mostly as LUTs) by using finite element analysis (FEA) or by conducting experiments in the laboratory. For many application (e.g. industrial drives), FEA data from the machine manufacturers may not be available to commissioning or control engineers but—as it is required for optimal controller tuning and operation of the

electrical drive system—machine identification [9] or self-commissioning [10] must be performed to extract (at least parts of) the flux linkage maps. To compensate for the nonlinear magnetic cross-coupling and saturation effects in the real-time control system with limit-storage, analytical functions instead of LUTs are preferable. Analytical functions are usually parameterized by a small number of parameters. Moreover, continuity and even differentiability of such functions over the whole operation range facilitate the derivation of differential inductances or the solution of analytical optimization problems [5].

Polynomial functions [11] are commonly adopted for representing the saturated flux linkages or differential inductances. Higher polynomial orders are necessary to enhance the fitting performance. Hence, a suitable polynomial order must be chosen according to the required estimation accuracy. To include the cross saturation into the models, bivariate polynomials [12], [13] could be used to avoid the need of saving several sets of parameters for different current regions. In [14], power functions, or so-called modified polynomial functions, with less parameters and a shared cross-coupling term are developed for describing the magnetic saturation of RSMs. The inverse (flux-current) relation is modeled here due to the similar curve shapes to the power function, which eases the fitting procedure. For identifying machine parameters automatically, based on [14], a self-commissioning method [15] for RSMs is developed by implementing a test injection sequence to improve the fitting process for the model. But several polynomial orders must be found to enhance the fitting results. Moreover, as the approach is not generic, the process has to be repeated for each individual machine. On the other hand, a few flux linkage prototype functions do exist. For example, [16] or [17] introduce novel RSM flux linkage approximation prototype functions, which are also able to reproduce self-axis saturation effects. The flux linkages are modeled separately by a linear and a nonlinear part. However, in particular for [16], several sets of parameters for different quadrature currents must be saved to cover the whole operation range. Therefore, a large numbers of parameters and the discontinuity of the prototype function limit its applicability. The prototype function in [17] is continuously differentiable but the accuracy is rather limited. For IPMSMs, a continuous prototype function is proposed in [3] to simplify the analysis of the saturation effects. But the saturation effects cannot be directly observed in the mathematical expressions due to its complexity with many reciprocal exponential functions. Furthermore, nonlinear flux maps are reduplicated by implementing artificial neural networks (ANNs) in [18]. Nevertheless, complex network structures result in complicated learning procedures and a large number of ANN parameters.

In [19], a rather simple analytical flux linkage prototype function for RSMs has been designed which achieves acceptable accuracy. But conservation of energy is not guaranteed. In this paper, this approach is extended and improved in order to obtain generic analytical flux linkage prototype functions for SMs in general (for RSMs and IPMSMs in particular). After presenting the nonlinear SM model covering saturation and cross-coupling effects, the first flux linkage prototype function for RSMs is presented which obeys the energy conservation (reciprocity) rule. As a consequence, the function not only meets physical requirements but also reduces the number of required parameters. Note that the coenergy variations due to cross-coupling effects should equal. However, small differences due to numerical (fitting) inaccuracies may occur but still allow for satisfactory approximation results. Afterwards, the second flux linkage prototype function is presented which can be applied for both RSMs and (I)PMSMs. Its generic structure allows to model any kind of nonlinear flux linkages of SMs with constant excitation, even those with permanent-magnet flux linkage component (offset) such as in IPMSMs.

Contributions of the paper are:

1) Flux linkage prototype functions for RSMs and IPMSMs are developed exploiting the intrinsic physical characteristics (such as Gaussian and sigmoid shapes) of nonlinear flux linkages of SMs instead of using polynomial functions or non-differentiable modulus (absolute value) functions; the resulting prototype functions are continuously differentiable, obey the energy conservation rule, have few parameters and can be extended in a generic and modular fashion (to meet arbitrarily high estimation accuracies).
2) Fitting procedures of the function parameters are designed in a step-by-step manner in order to effectively obtain an optimal set of parameters yielding best accuracy.
3) Effectiveness and accuracy of the proposed flux linkage prototype functions are evaluated and validated for real FEM-based and experimentally obtained flux linkage maps.

II. MODELING AND FLUX LINKAGE CHARACTERISTICS

First, the nonlinear model of SMs, used in this paper, is briefly revisited. Then, the flux linkages of RSMs and IPMSMs are studied and explained including self (direct) axis and cross (quadrature) axis saturation effects. Finally, the (differentiable) cross-coupling inductances are analyzed, which are crucial for a proper design of the proposed flux linkage prototype functions.

A. NONLINEAR MODEL OF SYNCHRONOUS MACHINES

Neglecting temperature, speed and position dependencies in the flux linkages, the electrical SM model in the rotating (d,q)-reference frame is given by [20, Chap. 14]

$$\boldsymbol{u}_\mathrm{s}^{dq} = R_\mathrm{s}\boldsymbol{i}_\mathrm{s}^{dq} + \omega_\mathrm{p}\underbrace{\begin{bmatrix}0 & -1\\ 1 & 0\end{bmatrix}}_{=:\boldsymbol{J}}\boldsymbol{\psi}_\mathrm{s}^{dq}(\boldsymbol{i}_\mathrm{s}^{dq}) + \tfrac{\mathrm{d}}{\mathrm{d}t}\boldsymbol{\psi}_\mathrm{s}^{dq}(\boldsymbol{i}_\mathrm{s}^{dq}) \quad (1)$$

where $\boldsymbol{u}_\mathrm{s}^{dq} := (u_\mathrm{s}^d, u_\mathrm{s}^q)^\top$ are the stator voltages (in V), $\boldsymbol{i}_\mathrm{s}^{dq} := (i_\mathrm{s}^d, i_\mathrm{s}^q)^\top$ are the stator currents (in A), $\boldsymbol{\psi}_\mathrm{s}^{dq} := (\psi_\mathrm{s}^d, \psi_\mathrm{s}^q)^\top$ are the flux linkages (in Wb; functions of $\boldsymbol{i}_\mathrm{s}^{dq}$) and R_s is the stator

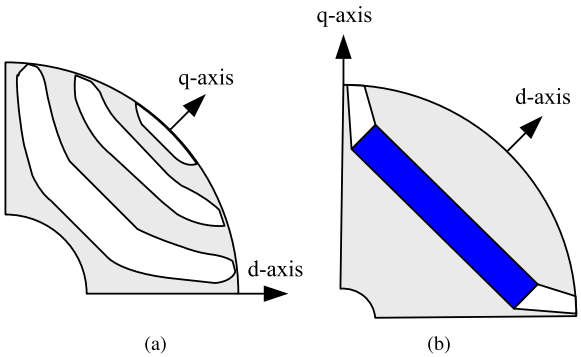

FIGURE 1. Principle rotor designs of the considered machines: (a) RSM rotor and (b) IPMSM rotor.

resistance (in Ω). The electric angular frequency $\omega_\mathrm{p} = n_\mathrm{p}\omega_\mathrm{m}$ (in rad/s) rotates the (d,q)-reference frame synchronously, where n_p and ω_m (in rad/s) denote the number of pole pairs and the mechanical angular frequency, respectively. The flux linkages can be expressed by

$$\boldsymbol{\psi}_\mathrm{s}^{dq}(\boldsymbol{i}_\mathrm{s}^{dq}) = \bar{\boldsymbol{\psi}}_\mathrm{s}^{dq}(\boldsymbol{i}_\mathrm{s}^{dq}) + \boldsymbol{\psi}_\mathrm{pm}^{dq} \tag{2}$$

where $\bar{\boldsymbol{\psi}}_\mathrm{s}^{dq} := (\bar{\psi}_\mathrm{s}^{d}, \bar{\psi}_\mathrm{s}^{q})^\top$ are stator flux linkage components due to the stator current excitation and $\boldsymbol{\psi}_\mathrm{pm}^{dq} := (\psi_\mathrm{pm}^{d}, \psi_\mathrm{pm}^{q})^\top$ are permanent magnet (PM) flux linkage components. Normally, $\boldsymbol{\psi}_\mathrm{pm}^{dq} := (\psi_\mathrm{pm}^{d}, 0)^\top$ can be used for PMSMs; in contrast, $\boldsymbol{\psi}_\mathrm{pm}^{dq} := (0, 0)^\top$ holds for RSMs.

For further derivations, the last term of (1) is rewritten as

$$\tfrac{\mathrm{d}}{\mathrm{d}t}\boldsymbol{\psi}_\mathrm{s}^{dq}(\boldsymbol{i}_\mathrm{s}^{dq}) = \tfrac{\partial \boldsymbol{\psi}_\mathrm{s}^{dq}(\boldsymbol{i}_\mathrm{s}^{dq})}{\partial \boldsymbol{i}_\mathrm{s}^{dq}} \tfrac{\mathrm{d}}{\mathrm{d}t}\boldsymbol{i}_\mathrm{s}^{dq} = \boldsymbol{L}_\mathrm{s}^{dq}(\boldsymbol{i}_\mathrm{s}^{dq}) \tfrac{\mathrm{d}}{\mathrm{d}t}\boldsymbol{i}_\mathrm{s}^{dq} \tag{3}$$

where the differential inductance matrix $\boldsymbol{L}_\mathrm{s}^{dq}$ (in H) is defined as the (partial) derivative of the flux linkages with respect to the stator currents, i.e.

$$\boldsymbol{L}_\mathrm{s}^{dq}(\boldsymbol{i}_\mathrm{s}^{dq}) := \begin{bmatrix} \frac{\partial \psi_\mathrm{s}^{d}(\boldsymbol{i}_\mathrm{s}^{dq})}{\partial i_\mathrm{s}^{d}} & \frac{\partial \psi_\mathrm{s}^{d}(\boldsymbol{i}_\mathrm{s}^{dq})}{\partial i_\mathrm{s}^{q}} \\ \frac{\partial \psi_\mathrm{s}^{q}(\boldsymbol{i}_\mathrm{s}^{dq})}{\partial i_\mathrm{s}^{d}} & \frac{\partial \psi_\mathrm{s}^{q}(\boldsymbol{i}_\mathrm{s}^{dq})}{\partial i_\mathrm{s}^{q}} \end{bmatrix} := \begin{bmatrix} L_\mathrm{s}^{d}(\boldsymbol{i}_\mathrm{s}^{dq}) & L_\mathrm{s}^{dq}(\boldsymbol{i}_\mathrm{s}^{dq}) \\ L_\mathrm{s}^{qd}(\boldsymbol{i}_\mathrm{s}^{dq}) & L_\mathrm{s}^{q}(\boldsymbol{i}_\mathrm{s}^{dq}) \end{bmatrix}. \tag{4}$$

B. FLUX LINKAGE CHARACTERISTICS

1) RSM

If iron losses are neglected, then, due to the symmetric rotor design of RSMs as shown in Fig. 1(a), the symmetry of the flux linkages with respect to the d-axis current i_s^{d} and q-axis current i_s^{q} implies

$$\begin{aligned} \psi_\mathrm{s}^{d}(i_\mathrm{s}^{d}, i_\mathrm{s}^{q}) &= -\psi_\mathrm{s}^{d}(-i_\mathrm{s}^{d}, i_\mathrm{s}^{q}), \\ \psi_\mathrm{s}^{q}(i_\mathrm{s}^{d}, i_\mathrm{s}^{q}) &= \psi_\mathrm{s}^{q}(-i_\mathrm{s}^{d}, i_\mathrm{s}^{q}) \end{aligned} \tag{5}$$

and

$$\begin{aligned} \psi_\mathrm{s}^{d}(i_\mathrm{s}^{d}, i_\mathrm{s}^{q}) &= \psi_\mathrm{s}^{d}(i_\mathrm{s}^{d}, -i_\mathrm{s}^{q}), \\ \psi_\mathrm{s}^{q}(i_\mathrm{s}^{d}, i_\mathrm{s}^{q}) &= -\psi_\mathrm{s}^{q}(i_\mathrm{s}^{d}, -i_\mathrm{s}^{q}), \end{aligned} \tag{6}$$

respectively. The real d-axis flux linkage ψ_s^{d} and q-axis flux linkage ψ_s^{q} of a 9.6 kW RSM are exemplarily shown in Fig. 2(a) and 2(b). Both axes (i.e. flux linkages and currents) are normalized with respect to their maximal values (i.e. $\psi_\mathrm{s}^{d/q}/\psi_\mathrm{s,max}^{d/q}$ (in Wb/Wb) and $i_\mathrm{s}^{d/q}/\widehat{i}_\mathrm{s,max}$ (in A/A)) and, then, plotted in the per unit (p.u.) system to ease comparability with other machines. The respective base (maximum) values of $\psi_\mathrm{s,max}^{d}$, $\psi_\mathrm{s,max}^{q}$ and $\widehat{i}_\mathrm{s,max}$ can be found in Table 2 in the appendix.

To illustrate and highlight the typical and intrinsic magnetic saturation effects of RSMs, Fig. 2(c) and 2(d) show the saturated self-axis flux linkage curves [——, ——, ——] extracted from the presented flux linkage maps in Fig. 2(a) and 2(b) for different cross-coupling currents. Even though flux curves in both d- and q-axes have similar trends, they illustrate different saturation effects. The d-axis flux linkage ψ_s^{d} saturates gradually in the higher current region after reaching the magnetic limit of the rotor laminations (e.g., iron steels). On the other hand, the q-axis flux linkage ψ_s^{q} saturates immediately in the lower current range, because the iron bridges located at the end of the flux barriers saturate easily; then it increases almost linearly with the current. To illustrate the typical cross-coupling saturation effects of RSMs, ψ_s^{d} over i_s^{q} and ψ_s^{q} over i_s^{d} [——, ——, ——] for different self-axis currents are plotted in Fig. 2(e) and 2(f), respectively. Obviously, both flux linkages are influenced by their respective cross-coupling currents. Compared to ψ_s^{q}, ψ_s^{d} is affected less by i_s^{q} due to the higher permeability in the d-axis flux path.

2) IPMSM

According to the rotor structure of IPMSMs shown in Fig. 1(b), the symmetry relation as in (6) only holds with respect to i_s^{q}. Due to the existence of PM materials in the d-axis, the flux linkage surfaces saturate asymmetrically with respect to the d-axis current. In Fig. 3(a) and 3(b), the real flux linkage maps (again in p.u.) of a 3.4 kW IPMSM are shown.

Its saturated self-axis flux linkages [——, ——, ——] are shown in Fig. 3(c) and 3(d). ψ_s^{d} is the sum of stator current flux linkage $\bar{\boldsymbol{\psi}}_\mathrm{s}^{dq}(\boldsymbol{i}_\mathrm{s}^{dq})$ and PM flux linkage $\boldsymbol{\psi}_\mathrm{pm}^{dq}$ (recall (2)). For positive i_s^{d}, it saturates gradually; in contrast, ψ_s^{d} for negative i_s^{d} (e.g. during field weakening), decreases almost linearly. On the other hand, ψ_s^{q} possesses a similar saturation effect as ψ_s^{d} of RSMs because the flux paths are similar. Fig. 3(e) and 3(f) illustrate the cross-coupling saturation effects [——, ——, ——]. Additionally, ψ_s^{d} over i_s^{q} for negative i_s^{d} is shown in Fig. 4, where different trends of the cross-coupling effects for positive and negative i_s^{d} can be observed in contrast to those for RSMs as was illustrated in Fig. 3(e). The symmetry in (6) of ψ_s^{d} with respect to i_s^{q} is clearly confirmed in Fig. 3(e) and 4; meanwhile, the asymmetry of ψ_s^{q} with respect to i_s^{d} can be observed in Fig. 3(f). Furthermore, by comparing Fig. 4 with Fig. 3(e) and the left part in Fig. 3(f) with the right, it can be seen that both ψ_s^{d} and ψ_s^{q} with negative i_s^{d} are less affected by cross-coupling saturation effects.

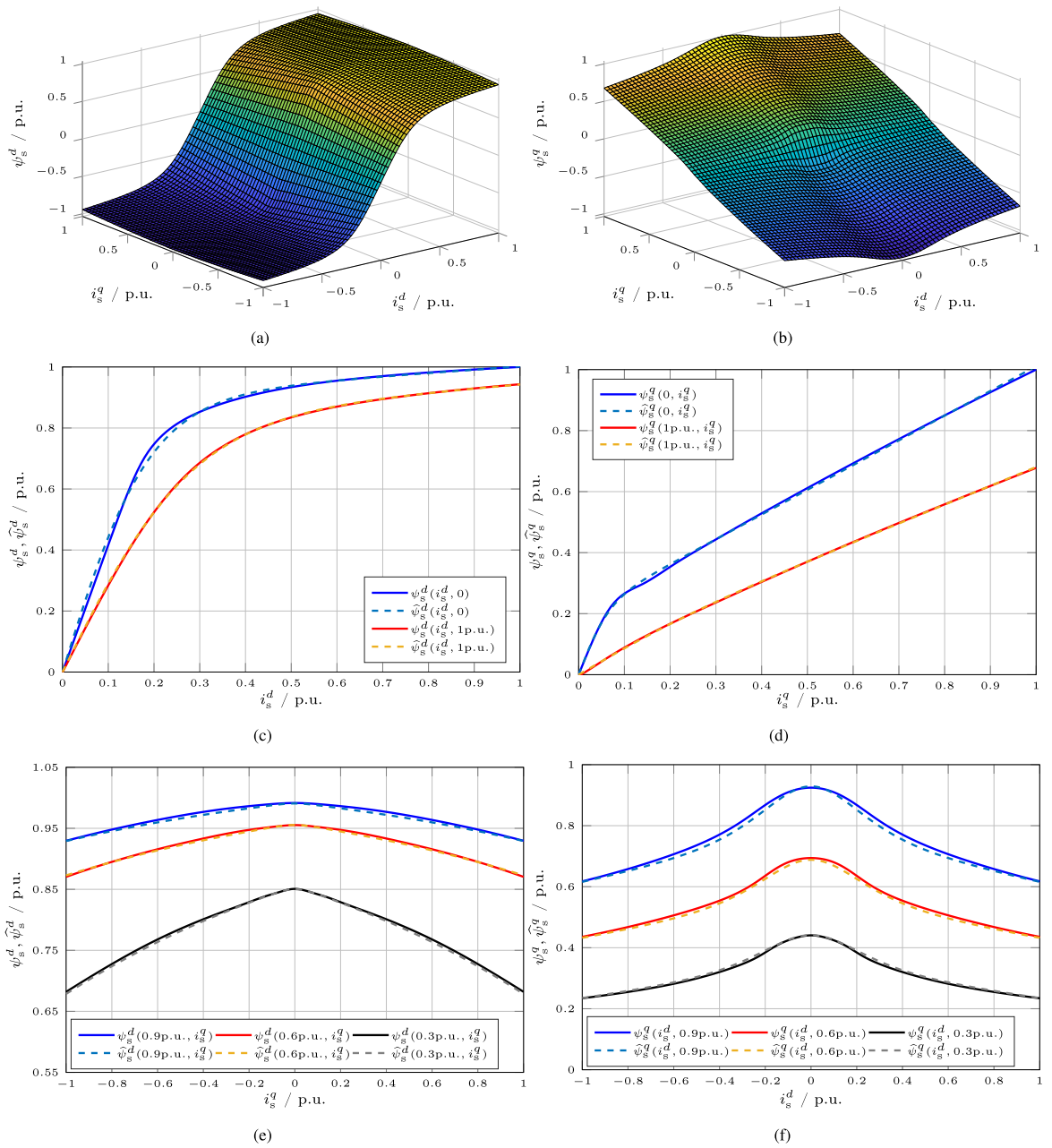

FIGURE 2. **Flux linkage characteristics of a 9.6 kW RSM: (a) real *d*-axis flux linkage map $\psi_s^d(i_s^d, i_s^q)$; (b) real *q*-axis flux linkage map $\psi_s^q(i_s^d, i_s^q)$; (c) real and approximated self-axis *d*-axis flux linkages $\psi_s^d(i_s^d, I_s^q)$ and $\widehat{\psi}_s^d(i_s^d, I_s^q)$ for different cross-coupling currents $i_s^q = I_s^q$; (d)real and approximated self-axis *q*-axis flux linkages $\psi_s^q(I_s^d, i_s^q)$ and $\widehat{\psi}_s^q(I_s^d, i_s^q)$ for different cross-coupling currents $i_s^d = I_s^d$; (e) real and approximated cross-coupling *d*-axis flux linkages $\psi_s^d(I_s^d, i_s^q)$ and $\widehat{\psi}_s^d(I_s^d, i_s^q)$ for different self-axis currents $i_s^d = I_s^d$; (f) real and approximated cross-coupling *q*-axis flux linkages $\psi_s^q(i_s^d, I_s^q)$ and $\widehat{\psi}_s^q(i_s^d, I_s^q)$ for different self-axis currents $i_s^q = I_s^q$ (where ψ_s^d and ψ_s^q [——, ——, ——] represent the real flux linkages, and $\widehat{\psi}_s^d$ and $\widehat{\psi}_s^q$ [- - -, - - -, - - -] represent their approximations as introduced in Section III).**

3) KEY OBSERVATIONS FOR PROTOTYPE FUNCTION DESIGN

From Fig. 2 (RSM) and Fig. 3 (IPMSM) several key and generic observations can be made. Even though different stator and rotor designs of RSMs and IPMSMs will result in different flux linkages, their shapes will be very similar. These similarities are in particularly apparent in the saturation trends in both self-axis and cross-coupling direction. Therefore, instead of fitting polynomials leading to several redundant parameters, designing physically motivated prototype functions to approximate and reflect these key observations is very meaningful.

To describe the self-axis saturation effects of the flux linkages, the sum of a hyperbolic function and a straight line, i.e.

$$\psi_{\mathrm{s,self}}^{d/q} \propto \tanh(i_{\mathrm{s}}^{d/q}) + i_{\mathrm{s}}^{d/q},$$

seems very well suited for RSMs as shown in Fig. 2(c) and 2(d) and also for IPMSMs as illustrated in Fig. 3(c) and 3(d);

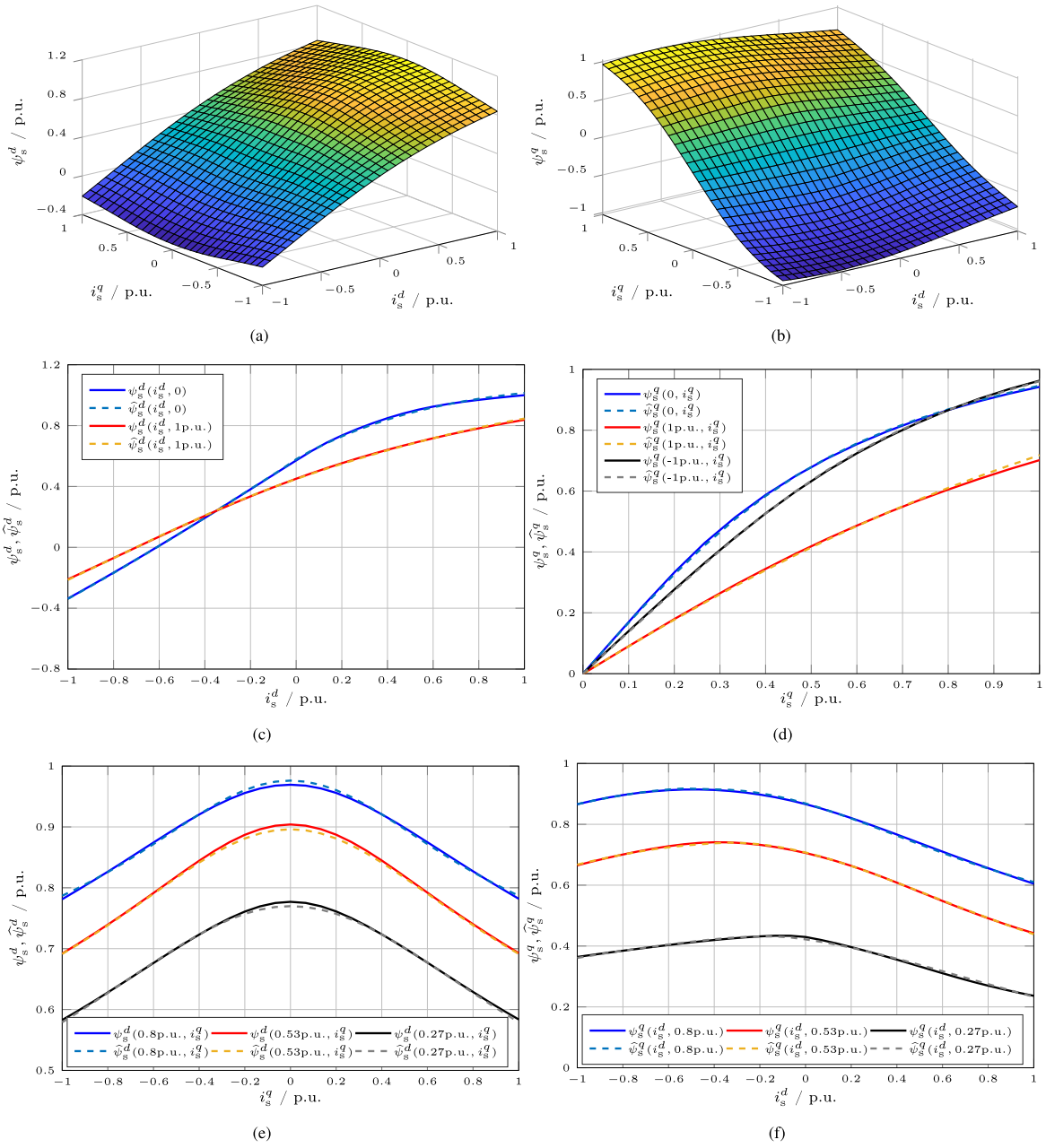

FIGURE 3. Flux linkage characteristics of a 3.4 kW IPMSM: (a) real *d*-axis flux linkage map $\psi_s^d(i_s^d, i_s^q)$; (b) real *q*-axis flux linkage map $\psi_s^q(i_s^d, i_s^q)$; (c) real and approximated self-axis *d*-axis flux linkages $\psi_s^d(i_s^d, I_s^q)$ and $\widehat{\psi}_s^d(i_s^d, I_s^q)$ for different cross-coupling currents $i_s^q = I_s^q$; (d) real and approximated self-axis *q*-axis flux linkages $\psi_s^q(I_s^d, i_s^q)$ and $\widehat{\psi}_s^q(I_s^d, i_s^q)$ for different cross-coupling currents $i_s^d = I_s^d$; (e) real and approximated cross-coupling *d*-axis flux linkages $\psi_s^d(I_s^d, i_s^q)$ and $\widehat{\psi}_s^d(I_s^d, i_s^q)$ for different self-axis currents $i_s^d = I_s^d$; (f) real and approximated cross-coupling *q*-axis flux linkages $\psi_s^q(i_s^d, I_s^q)$ and $\widehat{\psi}_s^q(i_s^d, I_s^q)$ for different self-axis currents $i_s^q = I_s^q$ (where ψ_s^d and ψ_s^q [——, ——, ——] represent the real flux linkages, and $\widehat{\psi}_s^d$ and $\widehat{\psi}_s^q$ [- - -, - - -, - - -] represent their approximations as introduced in Section V).

whereas to approximate the cross-coupling saturation effects, a (shifted) bell-shaped or Gaussian-like function, i.e.

$$\psi_{\mathrm{s,cross}}^{d/q} \propto -\ln\left(\cosh(i_{\mathrm{s}}^{d/q})\right) \text{ or } \psi_{\mathrm{s,cross}}^{d/q} \propto \exp\left(-(i_{\mathrm{s}}^{d/q})^2\right),$$

seems appropriate as illustrated in Fig. 2(e) & 2(f) for RSMs and in Fig. 3(e) & 4 for IPMSMs, respectively.

C. CROSS-COUPLING INDUCTANCE

By obeying the energy conservation rule, the well-known reciprocity relation is established, which means that mutual (differential) inductances must equal for two coupled inductors. Provided that losses are modeled separately, the reciprocity property holds true still in nonlinear synchronous machines (such as RSMs and IPMSMs) [21], i.e.,

$$L_{\mathrm{s}}^{dq}(\boldsymbol{i}_{\mathrm{s}}^{dq}) = L_{\mathrm{s}}^{qd}(\boldsymbol{i}_{\mathrm{s}}^{dq}) \text{ for all } \boldsymbol{i}_{\mathrm{s}}^{dq}. \tag{7}$$

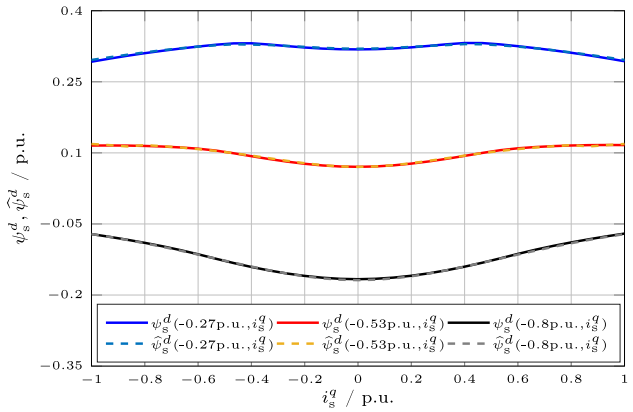

FIGURE 4. **IPMSM cross-coupling *d*-axis flux linkages $\psi_s^d(I_s^d, i_s^q)$ and $\hat{\psi}_s^d(I_s^d, i_s^q)$ for different self-axis currents $i_s^d = I_s^d < 0$ (where ψ_s^d [——, ——, ——] represents the real flux linkage and $\hat{\psi}_s^d$ [- - -, - - -, - - -] represents its approximation as introduced in Section V).**

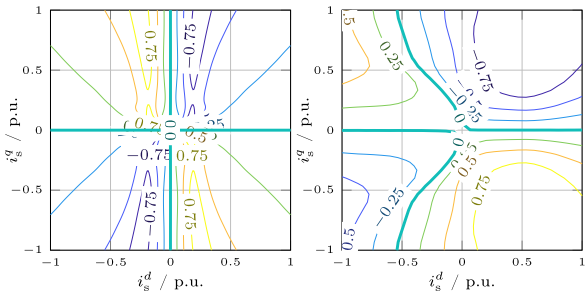

FIGURE 5. **Contour plots of cross-coupling differential inductances: (a) $\mathbb{L}_s^{dq}(L)$ of RSM (in p.u.); (b) $\mathbb{L}_s^{dq}(L)$ of IPMSM (in p.u.).**

To illustrate the characteristic of the differential cross-coupling inductances, the contour plot

$$\mathbb{L}_s^{dq}(L) := \{\boldsymbol{i}_s^{dq} \in \mathbb{R}^2 \mid L_s^{dq}(\boldsymbol{i}_s^{dq}) = L_s^{qd}(\boldsymbol{i}_s^{dq}) \stackrel{!}{=} L\}$$

of RSM and IPMSM, where $L_s^{dq} = L_s^{qd} = L$ holds with some given value $L \in \mathbb{R}$, are plotted in Fig. 5(a) and 5(b), respectively. All contour plots $\mathbb{L}_s^{dq}(L)$ are presented as p.u. plots as well, i.e. $\mathbb{L}_s^{dq}(L)/L_{s,\max}^{dq}$ (in H/H). One can observe the following common characteristics for both machines:

1) $L_s^{dq} = L_s^{qd} = L > 0$ are always positive in the upper-left and lower-right region (2nd and 4th quadrant) of the zero locus with $L = 0$ of the contour plot $\mathbb{L}_s^{dq}(0)$ (see green line).
2) $L_s^{dq} = L_s^{qd} = L < 0$ are always negative in the upper-right and lower-left region (1st and 3rd quadrant) of $\mathbb{L}_s^{dq}(0)$.

Analyzing the zero locus $\mathbb{L}_s^{dq}(0)$ with $L_s^{dq} = L_s^{qd} = 0$ (see Figs. 5, 6 and 10) yields the following observations:

1) The zero locus $\mathbb{L}_s^{dq}(0)$ exhibits an intersection at $\boldsymbol{i}_s^{dq} = (0, 0)^\top$.
2) The zero locus $\mathbb{L}_s^{dq}(0)$ separates the contour plots $\mathbb{L}_s^{dq}(L)$ for positive and negative L.
3) On the zero locus $\mathbb{L}_s^{dq}(0)$, ψ_s^d does not change along i_s^q and ψ_s^q does not change along i_s^d, respectively.

In Fig. 5(a), the zero locus $\mathbb{L}_s^{dq}(0)$ of the RSM is located on the axes where $i_s^q = 0$ and $i_s^d = 0$, since the flux linkages of the RSM are symmetric with respect to these axes (recall (5) and (6)). Moreover, every two adjacent quadrants have opposite signs but identical absolute values in their inductance values.

On the other hand, as shown in Fig. 5(b), the zero locus $\mathbb{L}_s^{dq}(0)$ of the IPMSM passes through the $i_s^q = 0$-axis but not through the $i_s^d = 0$-axis. In vertical direction parallel to the i_s^q-axis, it is curved and converges asymptotically to a vertical line at $i_s^d \approx -0.53$p.u. (not shown). Moreover, it is symmetric with respect to the $i_s^d = 0$-axis in the second and third quadrant. In conclusion, for (I)PMSMs, due to the existence of the PM, the vertical branch of the zero locus $\mathbb{L}_s^{dq}(0)$ moves from $i_s^d = 0$ (as for RSMs) to a constant negative i_s^d value ($i_s^d \approx -0.53$p.u. for the considered IPMSM).

III. RSM FLUX LINKAGE PROTOTYPE FUNCTION I

Now, the analytical flux linkage prototype functions of RSMs are derived. Afterwards, the fitting procedure is discussed in order to find a proper parametrization of the proposed prototype functions.

A. ANALYTICAL PROTOTYPE FUNCTION

As electrical machines are conservative systems, the energy during magnetization is not dissipated (if iron losses are neglected). The variation of coenergy $\Delta W_c(i_s^d, i_s^q)$ in both axes due to the cross-coupling saturation effect must equal [2]. Hence, the RSM flux linkages can be approximated by the following analytical prototype functions

$$\hat{\psi}_s^d(i_s^d, i_s^q) = \hat{\psi}_{s,\text{self}}^d(i_s^d) - \hat{\psi}_{s,\text{cross}}^d(i_s^d, i_s^q) \tag{8}$$

and

$$\hat{\psi}_s^q(i_s^d, i_s^q) = \hat{\psi}_{s,\text{self}}^q(i_s^q) - \hat{\psi}_{s,\text{cross}}^q(i_s^d, i_s^q), \tag{9}$$

where $\hat{\psi}_{s,\text{self}}^d(i_s^d)$ & $\hat{\psi}_{s,\text{self}}^q(i_s^q)$ and $\hat{\psi}_{s,\text{cross}}^d(i_s^d, i_s^q)$ & $\hat{\psi}_{s,\text{cross}}^q(i_s^d, i_s^q)$ represent *self-axis* and *cross-coupling* saturation terms, respectively. The overall flux linkages are obtained by subtracting the cross-coupling saturation terms from the self-axis saturation terms. The cross-coupling saturation terms can be modeled by the multiplication of two functions depending on only one current each, i.e.

$$\hat{\psi}_{s,\text{cross}}^d(i_s^d, i_s^q) = F'(i_s^d)G(i_s^q) \tag{10}$$

and

$$\hat{\psi}_{s,\text{cross}}^q(i_s^d, i_s^q) = F(i_s^d)G'(i_s^q), \tag{11}$$

where $F'(i_s^d) := \frac{\mathrm{d}}{\mathrm{d}i_s^d}F(i_s^d)$ and $G'(i_s^q) := \frac{\mathrm{d}}{\mathrm{d}i_s^q}G(i_s^q)$ denote the respective derivatives of the functions $F(i_s^d)$ and $G(i_s^q)$. With the definitions in (8), (9), (10) and (11), an identical coenergy

variation in both axes can be imposed resulting in

$$\Delta W_c(i_s^d, i_s^q) = \int \Big(\underbrace{\widehat{\psi}^d_{s,self}(i_s^d) - \widehat{\psi}^d_s(i_s^d, i_s^q)}_{=\widehat{\psi}^d_{s,cross}(i_s^d, i_s^q) = F'(i_s^d)G(i_s^q)} \Big) \, \mathrm{d}i_s^d$$

$$= \int \Big(\underbrace{\widehat{\psi}^q_{s,self}(i_s^q) - \widehat{\psi}^q_s(i_s^d, i_s^q)}_{=\widehat{\psi}^q_{s,cross}(i_s^d, i_s^q) = F(i_s^d)G'(i_s^q)} \Big) \, \mathrm{d}i_s^q = F(i_s^d)G(i_s^q). \quad (12)$$

Obviously, the reciprocity property is assured by the inherent structure of the chosen analytical functions, i.e., the partial derivatives of (8) and (9) with respect to the cross-coupling currents which must equal, i.e.

$$\frac{\mathrm{d}}{\mathrm{d}i_s^q} \widehat{\psi}^d_s(i_s^d, i_s^q) = \frac{\mathrm{d}}{\mathrm{d}i_s^d} \widehat{\psi}^q_s(i_s^d, i_s^q) = -F'(i_s^d)G'(i_s^q).$$

The RSM self-axis flux linkages in both axes for two constant cross currents are shown in Fig. 2(c) and 2(d) to illustrate the self-axis saturation characteristics. The self-axis saturation prototype (similarly designed as in [19]) employs a hyperbolic tangent function and a linear function to mimic the saturation effect in a single axis, which means that the flux linkages only dependent on one current (self-axis current). In view of Fig. 2(c) and 2(d) [——], the d- and q-axis self-axis saturation terms for zero cross-coupling current are defined as follows

$$\widehat{\psi}^d_{s,self}(i_s^d) := \widehat{\psi}^d_s(i_s^d, i_s^q = 0) := a_{d1} \tanh(a_{d2} i_s^d) + a_{d3} i_s^d \quad (13)$$

and

$$\widehat{\psi}^q_{s,self}(i_s^q) := \widehat{\psi}^q_s(i_s^d = 0, i_s^q) := a_{q1} \tanh(a_{q2} i_s^q) + a_{q3} i_s^q, \quad (14)$$

where a_{d1}, a_{d2} and a_{q1}, a_{q2} affect mainly the smooth transition before the linear region, and a_{d3} and a_{q3} describe the slope of the linear part of the prototype functions.

Afterwards, the cross-coupling saturation terms must be found. According to the required current range of the flux maps, maximum cross-coupling current constants I_{d1} and I_{q1} can be selected. By evaluating (8) and (9) at these maximum cross-coupling currents, the prototype functions simplify to

$$\widehat{\psi}^d_s(i_s^d, i_s^q = I_{q1}) = \widehat{\psi}^d_{s,self}(i_s^d) - F'(i_s^d)G(I_{q1}) \quad (15)$$

and

$$\widehat{\psi}^q_s(i_s^d = I_{d1}, i_s^q) = \widehat{\psi}^q_{s,self}(i_s^q) - F(I_{d1})G'(i_s^q), \quad (16)$$

which can be expressed with the self-axis saturation terms evaluated at I_{d1} and I_{q1} (as shown in Fig. 2(c) and 2(d) [——]), respectively, as

$$\widehat{\psi}^d_{s1}(i_s^d) := \widehat{\psi}^d_s(i_s^d, i_s^q = I_{q1}) := a_{d4} \tanh(a_{d5} i_s^d) + a_{d6} i_s^d \quad (17)$$

and

$$\widehat{\psi}^q_{s1}(i_s^q) := \widehat{\psi}^q_s(i_s^d = I_{d1}, i_s^q) := a_{q4} \tanh(a_{q5} i_s^q) + a_{q6} i_s^q, \quad (18)$$

where a_{d4}, a_{d5}, a_{d6} and a_{q4}, a_{q5}, a_{q6} have similar effects as the parameters defined in (13) and (14). Then, $\widehat{\psi}^d_s(i_s^d, i_s^q = I_{q1})$ and $\widehat{\psi}^q_s(i_s^d = I_{d1}, i_s^q)$ in (15) and (16) can be replaced by $\widehat{\psi}^d_{s1}(i_s^d)$ and $\widehat{\psi}^q_{s1}(i_s^q)$ from (17) and (18), respectively. Subsequently, the cross-coupling saturation terms $G(I_{q1})F'(i_s^d)$ and $F(I_{d1})G'(i_s^q)$ in (15) and (16) can be obtained by computing the differences $\widehat{\psi}^d_{s,self}(i_s^d) - \widehat{\psi}^d_{s1}(i_s^d)$ and $\widehat{\psi}^q_{s,self}(i_s^q) - \widehat{\psi}^q_{s1}(i_s^q)$ as follows

$$G(I_{q1})F'(i_s^d) = a_{d1} \tanh(a_{d2} i_s^d) + a_{d3} i_s^d - a_{d4} \tanh(a_{d5} i_s^d) - a_{d6} i_s^d \quad (19)$$

and

$$F(I_{d1})G'(i_s^q) = a_{q1} \tanh(a_{q2} i_s^q) + a_{q3} i_s^q - a_{q4} \tanh(a_{q5} i_s^q) - a_{q6} i_s^q, \quad (20)$$

respectively. Integration of both equations yields

$$G(I_{q1})F(i_s^d) = \frac{1}{2}(a_{d3} - a_{d6})(i_s^d)^2 + \frac{a_{d1}}{a_{d2}} \ln\Big(\cosh(a_{d2} i_s^d)\Big) - \frac{a_{d4}}{a_{d5}} \ln\Big(\cosh(a_{d5} i_s^d)\Big) \quad (21)$$

and

$$F(I_{d1})G(i_s^q) = \frac{1}{2}(a_{q3} - a_{q6})(i_s^q)^2 + \frac{a_{q1}}{a_{q2}} \ln\Big(\cosh(a_{q2} i_s^q)\Big) - \frac{a_{q4}}{a_{q5}} \ln\Big(\cosh(a_{q5} i_s^q)\Big), \quad (22)$$

which clearly gives continuously differentiable functions.

Until now, all parts of the prototype functions are found. The cross-saturation terms $F'(i_s^d)G(i_s^q)$ and $F(i_s^d)G'(i_s^q)$ can be acquired by multiplying (19) and (22), and (20) and (21), respectively. The entire RSM flux linkage prototype functions as in (8) and (9) are finally given by

$$\widehat{\psi}^d_s(i_s^d, i_s^q) = \widehat{\psi}^d_{s,self}(i_s^d) - \underbrace{\frac{1}{F(I_{d1})G(I_{q1})} \Big(G(I_{q1})F'(i_s^d)\Big)\Big(F(I_{d1})G(i_s^q)\Big)}_{\overset{(10)}{=} \widehat{\psi}^d_{s,cross}(i_s^d, i_s^q)} \quad (23)$$

and

$$\widehat{\psi}^q_s(i_s^d, i_s^q) = \widehat{\psi}^q_{s,self}(i_s^q) - \underbrace{\frac{1}{F(I_{d1})G(I_{q1})} \Big(G(I_{q1})F(i_s^d)\Big)\Big(F(I_{d1})G'(i_s^q)\Big)}_{\overset{(11)}{=} \widehat{\psi}^q_{s,cross}(i_s^d, i_s^q)}. \quad (24)$$

In the explicit form of the prototype functions, it can be concluded that $F(i_s^d)$ and $G(i_s^q)$ (derived in (21) and (22)) describe how the cross-coupling currents affect the flux linkage values; whereas $F'(i_s^d)$ and $G'(i_s^q)$ (derived in (19) and (20)) control the extent of the cross-coupling saturation effect under different current levels and allow to specify the "opening width" of the bell-shaped functions $F(i_s^d)$ and $G(i_s^q)$ as is illustrated in Fig. 2(e) and 2(f). Note that all equations from (19) to (22) depend on $F(I_{d1})$ and/or $G(I_{q1})$. However, the product

$F(I_{\mathrm{d1}})G(I_{\mathrm{q1}})$ in (23) and (24) can be eliminated after a successful fitting process.

B. FITTING PROCEDURE

A fitting procedure is presented which allows to find proper (optimal) parameters of the proposed analytical flux linkage prototype function. First, in total four functions – the self saturated terms $\widehat{\psi}^{d}_{\mathrm{s,self}}(i^{d}_{\mathrm{s}})$, $\widehat{\psi}^{q}_{\mathrm{s,self}}(i^{q}_{\mathrm{s}})$ without the cross saturation effect and the terms $\widehat{\psi}^{d}_{\mathrm{s1}}(i^{d}_{\mathrm{s}})$, $\widehat{\psi}^{q}_{\mathrm{s1}}(i^{q}_{\mathrm{s}})$ with the cross saturation effect – must be fitted.

To do so, the MATLAB nonlinear regression function *nlinfit* with the Levenberg-Marquardt algorithm (LMA) [22] is adopted for finding proper parameters $a_{\mathrm{d1}},\ldots,a_{\mathrm{d6}}$ and $a_{\mathrm{q1}},\ldots,a_{\mathrm{q6}}$ in (13), (14), (17) and (18). The optimal fitting parameters of the prototype functions are found by minimizing the following four nonlinear least square problems

$$\min_{a_{\mathrm{d1}},a_{\mathrm{d2}},a_{\mathrm{d3}}} \sum_{j=1}^{m} \left[\psi^{d}_{\mathrm{s}}(i^{d}_{\mathrm{s},j},0) - \widehat{\psi}^{d}_{\mathrm{s,self}}(i^{d}_{\mathrm{s},j},a_{\mathrm{d1}},a_{\mathrm{d2}},a_{\mathrm{d3}}) \right]^2 \tag{25}$$

$$\min_{a_{\mathrm{q1}},a_{\mathrm{q2}},a_{\mathrm{q3}}} \sum_{k=1}^{n} \left[\psi^{q}_{\mathrm{s}}(0,i^{q}_{\mathrm{s},k}) - \widehat{\psi}^{q}_{\mathrm{s,self}}(i^{q}_{\mathrm{s},k},a_{\mathrm{q1}},a_{\mathrm{q2}},a_{\mathrm{q3}}) \right]^2 \tag{26}$$

$$\min_{a_{\mathrm{d4}},a_{\mathrm{d5}},a_{\mathrm{d6}}} \sum_{j=1}^{m} \left[\psi^{d}_{\mathrm{s}}(i^{d}_{\mathrm{s},j},I_{\mathrm{q1}}) - \widehat{\psi}^{d}_{\mathrm{s1}}(i^{d}_{\mathrm{s},j},a_{\mathrm{d4}},a_{\mathrm{d5}},a_{\mathrm{d6}}) \right]^2 \tag{27}$$

$$\min_{a_{\mathrm{q4}},a_{\mathrm{q5}},a_{\mathrm{q6}}} \sum_{k=1}^{n} \left[\psi^{q}_{\mathrm{s}}(I_{\mathrm{d1}},i^{q}_{\mathrm{s},k}) - \widehat{\psi}^{q}_{\mathrm{s1}}(i^{q}_{\mathrm{s},k},a_{\mathrm{q4}},a_{\mathrm{q5}},a_{\mathrm{q6}}) \right]^2 \tag{28}$$

where $i^{d}_{\mathrm{s},j}$, $i^{q}_{\mathrm{s},k}$ are the j-th and k-th current data points of the real flux linkage values ψ^{d}_{s} and ψ^{q}_{s} which are used as reference. After finding these 12 parameters, also the value of coenergy variation $\Delta W_{\mathrm{c}}(I_{\mathrm{d1}},I_{\mathrm{q1}})$ can be found which finally allows to approximate the real flux linkages by the analytical and (now) parametrized flux linkage prototype functions (8) and (9).

C. APPROXIMATION RESULTS

The first analytical flux linkage prototype function in (8) and (9) obey the energy conservation rule and now are used to mimic the magnetic nonlinearity of an RSM. The real flux maps of a custom-built highly nonlinear 9.6 kW RSM (Courtesy of Prof. Maarten Kamper, Stellenbosch University, ZA) are employed as reference. Its parameters are collected in Table 2 in the appendix. The real flux linkage values of the RSM are used to fit the flux linkage prototypes (8) and (9) by obtaining an optimal parameter set for $a_{\mathrm{d1}},\ldots,a_{\mathrm{d6}}$ and $a_{\mathrm{q1}},\ldots,a_{\mathrm{q6}}$. The fitted parameters are provided in Table 3 in the appendix. Maximal cross-coupling current constants $I_{\mathrm{d1}} = I_{\mathrm{q1}} = 1\mathrm{p.u.}$ are selected. Ideally, the coenergy variations at the maximum currents, i.e. $\Delta W_{\mathrm{c}}(I_{\mathrm{d1}},I_{\mathrm{q1}}) = F(I_{\mathrm{d1}})G(I_{\mathrm{q1}})$, must be equal in both axes due to the energy conservation rule as shown in (12). However, after fitting, $G(I_{\mathrm{q1}})F(I_{\mathrm{d1}}) = 4.35$ and $F(I_{\mathrm{d1}})G(I_{\mathrm{q1}}) = 4.29$ are obtained which slightly differ, although according to (21) and (22) both should equal. So their average value is used in the following. In practice, the small difference may result from numerical inaccuracies in the experimental data and the flux linkage interpolation. Nevertheless, this small difference is still acceptable for the design of the flux linkage prototype functions as will be shown in the following. Due to the symmetry of the flux linkages and the designed prototype functions, only the flux linkage samples in the first quadrant are needed for parameter fitting. The analytical prototype function directly allows to extended the approximation results to the whole operation range including all four quadrants.

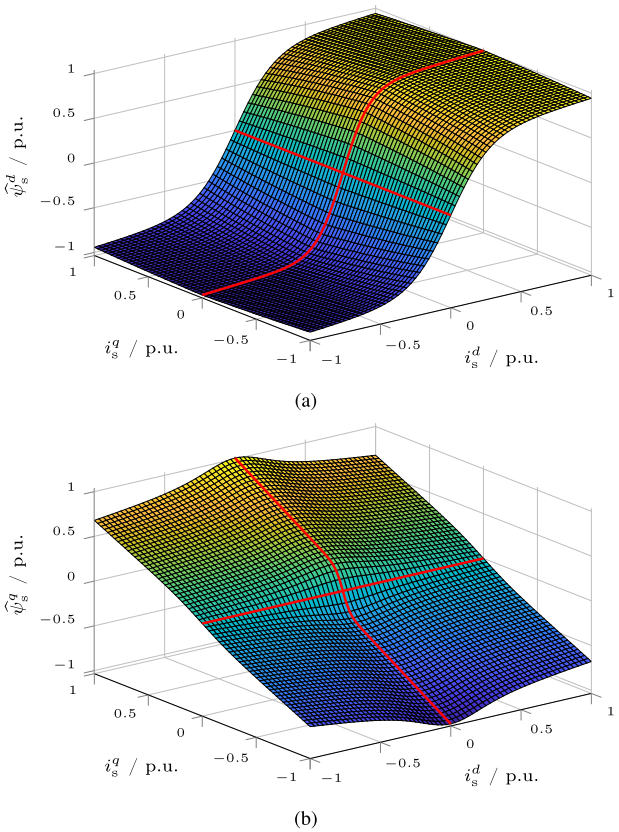

FIGURE 6. Approximation results of the proposed analytical flux linkage prototype functions (8) and (9): (a) fitted *d*-axis flux linkage $\widehat{\psi}^{d}_{\mathrm{s}}$; (b) fitted *q*-axis flux linkage $\widehat{\psi}^{q}_{\mathrm{s}}$; zero locus $\mathbb{L}^{dq}_{\mathrm{s}}(L=0)$ [——] is indicated.

The fitted d-axis flux linkage $\widehat{\psi}^{d}_{\mathrm{s}}$ and q-axis flux linkage $\widehat{\psi}^{q}_{\mathrm{s}}$ are shown in Fig. 6(a) and 6(b), respectively. $\widehat{\psi}^{d}_{\mathrm{s}}$ and $\widehat{\psi}^{q}_{\mathrm{s}}$ are shown in the p.u. system again, i.e. $\widehat{\psi}^{d/q}_{\mathrm{s}}/\psi^{d/q}_{\mathrm{s,max}}$ (in Wb/Wb). It can be seen that both flux maps possess continuously differentiable surfaces. Moreover, (very) good approximation results [- - -, - - -, - - -] of the designed self-axis prototype functions (13), (14), (17) and (18) are confirmed in Fig. 2(c) and 2(d). On the other hand, under different conditions, Fig. 2(e) and 2(f) illustrate the capability of the proposed prototype

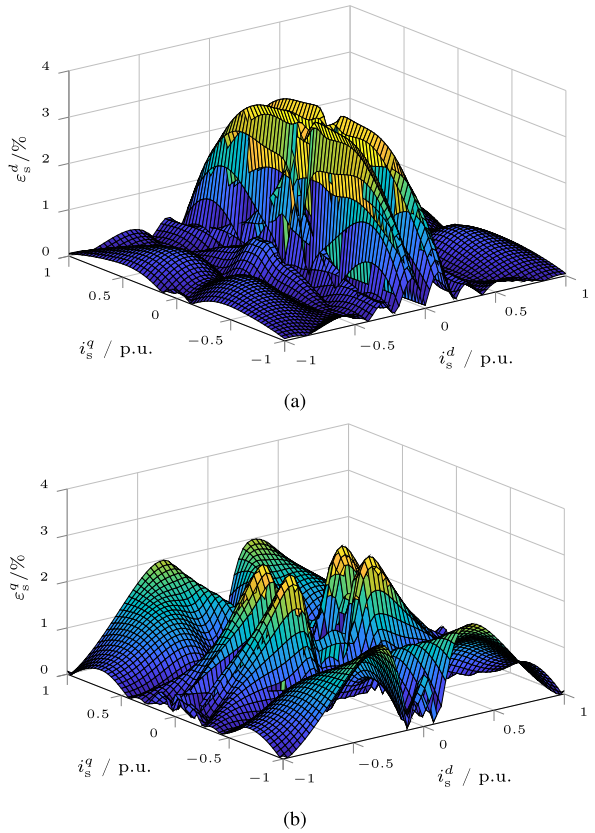

FIGURE 7. Approximation errors of the proposed analytical flux linkage prototype functions (8) and (9) compared to the real flux linkage maps: (a) normalized *d*-axis error ε_s^d; (b) normalized *q*-axis error ε_s^q.

functions to model the cross saturation effects and to obey the reciprocity property (7).

To quantify the approximation (fitting) accuracy, the normalized approximation error

$$\varepsilon_s^{d/q} := \frac{|\psi_s^{d/q} - \hat{\psi}_s^{d/q}|}{\psi_{s,\max}^{d/q}} \cdot 100\% \tag{29}$$

is introduced, where $\hat{\psi}_s^d$ and $\hat{\psi}_s^q$ are the estimated flux linkages, ψ_s^d and ψ_s^q are the real flux linkages and $\psi_{s,\max}^d$ and $\psi_{s,\max}^q$ are the maximum real values of the d- and q-components. Fig. 7(a) and 7(b) show the normalized errors ε_s^d and ε_s^q, respectively. The error plots indicate a fitting accuracy of at least 96.5% in the whole current range; therefore, the nonlinear flux linkages of the considered RSM are properly approximated by the proposed flux linkage prototype functions (8) and (9).

In Fig. 9(a), 9(b) and 9(c), the differential inductances L_s^d, L_s^q and L_s^{dq} (again in p.u.), computed by numerical differentiation of the real flux linkages, are shown. The approximated differential inductances $\hat{L}_s^d = \frac{\partial \hat{\psi}_s^d(\boldsymbol{i}_s^{dq})}{\partial i_s^d}$, $\hat{L}_s^q = \frac{\partial \hat{\psi}_s^q(\boldsymbol{i}_s^{dq})}{\partial i_s^q}$ and $\hat{L}_s^{dq} = \frac{\partial \hat{\psi}_s^d(\boldsymbol{i}_s^{dq})}{\partial i_s^q} = \frac{\partial \hat{\psi}_s^q(\boldsymbol{i}_s^{dq})}{\partial i_s^d}$, derived by analytical differentiation of the flux linkage prototype functions in (8) and (9), are shown in Fig. 9(d), 9(e) and 9(f), respectively. Due to the continuous differentiability of the prototype functions, well-fitted and continuous inductances are obtained which might be used for nonlinear/adaptive current controllers [4] or optimal feedforward torque control [5].

In conclusion, the simple fitting procedure presented here results in good approximation results while solely the four self-axis functions, i.e., (25)–(28), were fitted separately instead of the entire flux linkage surfaces. Nevertheless, the prototype functions (8) and (9) incorporate the more complicated integrated parts in (21) and (22). As a consequence, an additional fitting step, which makes use of a fitting procedure covering the whole flux linkage maps at once seems promising but requires a relatively long convergence time and might lead to even worse fitting results (at certain current pairs). These two bottlenecks are further studied and overcome in the next sections.

IV. RSM FLUX LINKAGE PROTOTYPE FUNCTION II

The proposed RSM prototype function I is rather static and lacks flexibility for extension and application to other machines. Therefore, in this section, from the gained knowledge, another improved RSM flux linkage prototype function is presented.

A. ANALYTICAL PROTOTYPE FUNCTION

To easily refer to the modified RSM model in the following derivation, the identical structures of the flux linkage prototypes as in (8) and (9) are reused, i.e.

$$\hat{\psi}_s^d(i_s^d, i_s^q) = \hat{\psi}_{s,\text{self}}^d(i_s^d) - \hat{\psi}_{s,\text{cross}}^d(i_s^d, i_s^q) \tag{30}$$

and

$$\hat{\psi}_s^q(i_s^d, i_s^q) = \hat{\psi}_{s,\text{self}}^q(i_s^q) - \hat{\psi}_{s,\text{cross}}^q(i_s^d, i_s^q), \tag{31}$$

where $\hat{\psi}_{s,\text{cross}}^d$ and $\hat{\psi}_{s,\text{cross}}^q$ again represent cross-coupling saturation terms but now are modified to the following more general form

$$\hat{\psi}_{s,\text{cross}}^d(i_s^d, i_s^q) = k_1 F_1'(i_s^d) G_1(i_s^q) + \cdots + k_n F_n'(i_s^d) G_n(i_s^q) \tag{32}$$

and

$$\hat{\psi}_{s,\text{cross}}^q(i_s^d, i_s^q) = k_1 F_1(i_s^d) G_1'(i_s^q) + \cdots + k_n F_n(i_s^d) G_n'(i_s^q) \tag{33}$$

where $k_1, \ldots, k_n$ are cross-coupling saturation constants, $F_1, \ldots, F_n$ and $G_1, \ldots, G_n$ describe the cross-coupling saturation effects and $F_1', \ldots, F_n'$ and $G_1', \ldots, G_n'$ control the impact of the cross-coupling saturation effect for different current levels on the prototype function. The number n of cross-coupling saturation terms in (32) and (33) may be chosen arbitrarily to meet given accuracy requirements. With adequately chosen prototype terms, $n = 3$ or $n = 4$ usually give satisfactory fitting accuracies.

The self-axis saturation terms $\hat{\psi}_{s,\text{self}}^d$ and $\hat{\psi}_{s,\text{self}}^q$ as introduced in (13) and (14) will be adopted again. The design of $\hat{\psi}_{s,\text{cross}}^d$ and $\hat{\psi}_{s,\text{cross}}^q$ is the main task now. A Gaussian function, which possesses a symmetric and bell-shaped curve, is

a good candidate for describing the cross-coupling saturation effect (recall Fig. 2(e) and 2(f)). Hence a modified Gaussian function, which is negative and shifted upward, is used here, so the flux linkages can decrease gradually from the origin due to the increase of the cross-coupling current. In order to obtain a better fitting performance, $n = 4$ is chosen; resulting four modified Gaussian functions and cross-coupling saturation terms $F_1(i_\mathrm{s}^d), \ldots, F_4(i_\mathrm{s}^d)$ and $G_1(i_\mathrm{s}^q), \ldots, G_4(i_\mathrm{s}^q)$, which describe how i_s^d affects ψ_s^q and how i_s^q affects ψ_s^d, respectively, are chosen as

$$F_1(i_\mathrm{s}^d) = 1 - e^{-\left(a_{\mathrm{d}4}\, i_\mathrm{s}^d\right)^2}, \ldots, F_4(i_\mathrm{s}^d) = 1 - e^{-\left(a_{\mathrm{d}7}\, i_\mathrm{s}^d\right)^2} \quad (34)$$

and

$$G_1(i_\mathrm{s}^q) = 1 - e^{-\left(a_{\mathrm{q}4} i_\mathrm{s}^q\right)^2}, \ldots, G_4(i_\mathrm{s}^q) = 1 - e^{-\left(a_{\mathrm{q}7} i_\mathrm{s}^q\right)^2}, \quad (35)$$

where $a_{\mathrm{d}4}, a_{\mathrm{d}5}, a_{\mathrm{d}6}, a_{\mathrm{d}7}$ and $a_{\mathrm{q}4}, a_{\mathrm{q}5}, a_{\mathrm{q}6}, a_{\mathrm{q}7}$ control the widths of the corresponding Gaussian functions. The derivatives of (34) and (35) are given by

$$F_1'(i_\mathrm{s}^d) = 2a_{\mathrm{d}4}^2 i_\mathrm{s}^d e^{-(a_{\mathrm{d}4} i_\mathrm{s}^d)^2}, \ldots, F_4'(i_\mathrm{s}^d) = 2a_{\mathrm{d}7}^2 i_\mathrm{s}^d e^{-(a_{\mathrm{d}7} i_\mathrm{s}^d)^2} \quad (36)$$

and

$$G_1'(i_\mathrm{s}^q) = 2a_{\mathrm{q}4}^2 i_\mathrm{s}^q e^{-(a_{\mathrm{q}4} i_\mathrm{s}^q)^2}, \ldots, G_4'(i_\mathrm{s}^q) = 2a_{\mathrm{q}7}^2 i_\mathrm{s}^q e^{-(a_{\mathrm{q}7} i_\mathrm{s}^q)^2}. \quad (37)$$

Note that the extent of the cross-coupling saturation effect clearly varies for different self- and cross-coupling currents due to products of $F_\mathrm{i}'(i_\mathrm{s}^d)G_\mathrm{i}(i_\mathrm{s}^q)$ and $F_\mathrm{i}(i_\mathrm{s}^d)G_\mathrm{i}'(i_\mathrm{s}^q)$ in (32) and (33), respectively.

B. FITTING PROCEDURE

For the more generic RSM flux linkage prototype function II, a modified fitting procedure must be applied. As the self-axis saturation terms $\widehat{\psi}_{\mathrm{s,self}}^d$ and $\widehat{\psi}_{\mathrm{s,self}}^q$ introduced in (13) and (14) are used again, also the fitting procedure to find the parameters $a_{\mathrm{d}1}, a_{\mathrm{d}2}, a_{\mathrm{d}3}$ and $a_{\mathrm{q}1}, a_{\mathrm{q}2}, a_{\mathrm{q}3}$ can be reused by solving (25) and (26). Afterwards, the parameters taking into account the cross-coupling saturation effect in $\widehat{\psi}_{\mathrm{s,cross}}^d$ and $\widehat{\psi}_{\mathrm{s,cross}}^q$ must be found. The flux linkage curves which contain dominant cross-coupling saturation effects must be extracted as references by subtracting the real flux linkages from the fitted self-axis saturation curves. The two d- and q-axis flux linkage terms must be fitted at the same time by solving the following minimization problem

$$\min_{\boldsymbol{a}_{\mathrm{dq}}} \sum_{j=1}^{m}\sum_{k=1}^{n}\left[\psi_{\mathrm{s,cross}}^d(i_{\mathrm{s},j}^d, i_{\mathrm{s},k}^q) - \widehat{\psi}_{\mathrm{s,cross}}^d(i_{\mathrm{s},j}^d, i_{\mathrm{s},k}^q, \boldsymbol{a}_{\mathrm{dq}}^{\mathrm{red}})\right]^2 + \left[\psi_{\mathrm{s,cross}}^q(i_{\mathrm{s},j}^d, i_{\mathrm{s},k}^q) - \widehat{\psi}_{\mathrm{s,cross}}^q(i_{\mathrm{s},j}^d, i_{\mathrm{s},k}^q, \boldsymbol{a}_{\mathrm{dq}}^{\mathrm{red}})\right]^2 \quad (38)$$

where $\psi_{\mathrm{s,cross}}^d$ & $\psi_{\mathrm{s,cross}}^q$ are the real cross-coupling saturation flux linkage terms and

$$\boldsymbol{a}_{\mathrm{dq}}^{\mathrm{red}} = (a_{\mathrm{d}4}, a_{\mathrm{d}5}, a_{\mathrm{d}6}, a_{\mathrm{d}7}, a_{\mathrm{q}4}, a_{\mathrm{q}5}, a_{\mathrm{q}6}, a_{\mathrm{q}7}, k_1, k_2, k_3, k_4)^\top$$

collects the reduced number of fitting parameters as in (32) and (33).

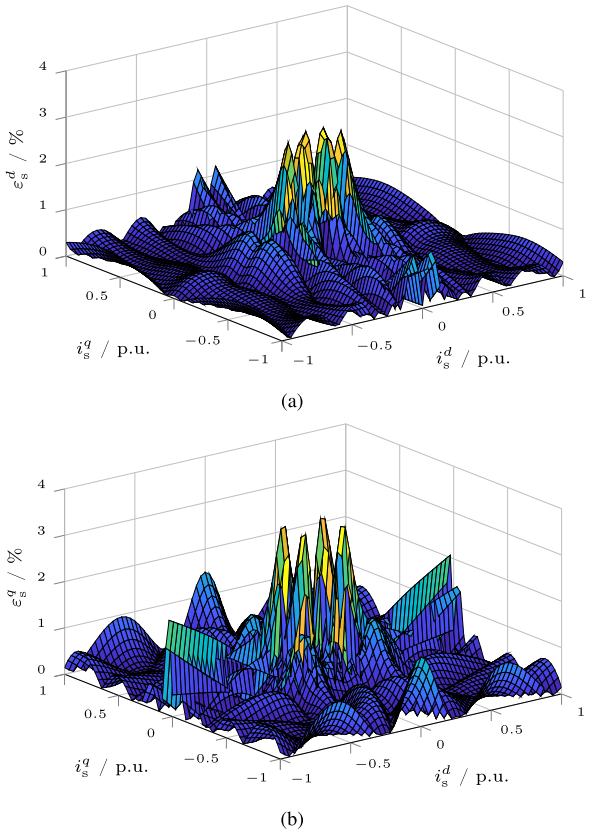

FIGURE 8. Approximation errors of the proposed analytical flux linkage prototype functions (30) and (31) compared to the real flux maps: (a) normalized *d*-axis error ε_s^d; (b) normalized *q*-axis error ε_s^q.

In order to compensate for the induced errors by the previous separated fitting procedure and to achieve a better fitting accuracy, the already fitted parameters in $\boldsymbol{a}_{\mathrm{dq}}^{\mathrm{red}}$ are used as initial values (guesses) for another fitting iteration where self- *and* cross-coupling terms in (30) and (31) are fitted at once to find the remaining and the (globally) optimal parameters. The use of the initial values effectively shortens the convergence time of fitting procedure. The overall minimization problem now is as follows

$$\min_{\boldsymbol{a}_{\mathrm{dq}}} \sum_{j=1}^{m}\sum_{k=1}^{n}\left[\psi_\mathrm{s}^d(i_{\mathrm{s},j}^d, i_{\mathrm{s},k}^q) - \widehat{\psi}_\mathrm{s}^d(i_{\mathrm{s},j}^d, i_{\mathrm{s},k}^q, \boldsymbol{a}_{\mathrm{dq}})\right]^2 + \left[\psi_\mathrm{s}^q(i_{\mathrm{s},j}^d, i_{\mathrm{s},k}^q) - \widehat{\psi}_\mathrm{s}^q(i_{\mathrm{s},j}^d, i_{\mathrm{s},k}^q, \boldsymbol{a}_{\mathrm{dq}})\right]^2 \quad (39)$$

where

$$\boldsymbol{a}_{\mathrm{dq}} = (a_{\mathrm{d}1}, \ldots, a_{\mathrm{d}7}, a_{\mathrm{q}1}, \ldots, a_{\mathrm{q}7}, k_1, k_2, k_3, k_4)^\top$$

incorporates now *all* fitting parameters of the flux linkage prototype functions proposed in (30) and (31).

C. APPROXIMATION RESULTS

The real RSM introduced in the last section is reused to evaluate the second RSM flux linkage prototype function. The fitted parameters are listed in Table 3 in the appendix.

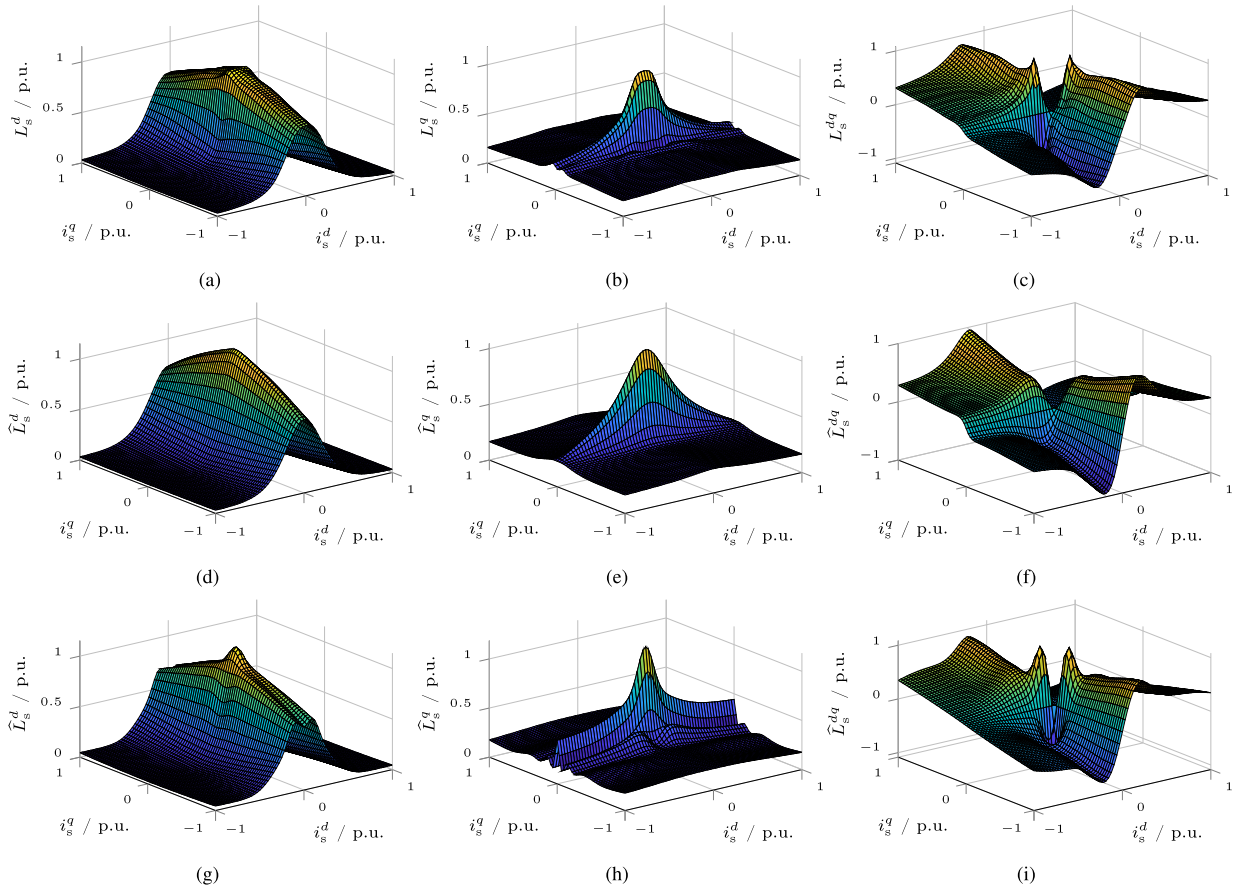

FIGURE 9. Differential inductances of the considered RSM: (a) real *d*-axis differential inductance L_s^d; (b) real *q*-axis differential inductance L_s^q; (c) real cross-coupling differential inductance L_s^{dq}; (d) approximated *d*-axis differential inductance $\widehat{L}_s^d$ derived from (8) and (9); (e) approximated *q*-axis differential inductance $\widehat{L}_s^q$ derived from (8) and (9); (f) approximated cross-coupling differential inductance $\widehat{L}_s^{dq}$ derived from (8) and (9); (g) approximated *d*-axis differential inductance $\widehat{L}_s^d$ derived from (30) and (31); (h) approximated *q*-axis differential inductance $\widehat{L}_s^q$ derived from (30) and (31); (i) approximated cross-coupling differential inductance $\widehat{L}_s^{dq}$ derived from (30) and (31).

As the fitting results are similar to the results obtained by the RSM flux linkage prototype function I, the approximated flux linkage maps using (30) and (31) are not plotted again. The normalized errors ε_s^d and ε_s^q are shown in Fig. 8(a) and 8(b), respectively. Again good fitting accuracies were feasible. In comparison to the RSM prototype function I, both ε_s^d and ε_s^q of the RSM prototype function II were reduced significantly. The cross-coupling saturation effects are approximated in a much better fashion by the four modified Gaussian functions in (32) and (33). Some error peaks remain but are acceptable.

Besides the flux linkages, in Fig. 9(g), 9(h) and 9(i), the approximated differential inductances $\widehat{L}_\mathrm{s}^d$, $\widehat{L}_\mathrm{s}^q$ and $\widehat{L}_\mathrm{s}^{dq}$, derived by analytical differentiation of the fitted prototype functions in (30) and (31), are shown. Due to the generic nature of the chosen prototype functions and the overall fitting process, the differential inductances derived from the RSM prototype function II can represent the peak-like changes of the real differential inductances better than those from the RSM prototype function I. Without any additional design of separate inductance prototype functions, the partial derivatives of the proposed flux linkage prototype functions directly allow to compute analytical approximations of the differential inductances with quite high accuracy.

In conclusion, both proposed flux linkage approximations can present well the severe magnetic nonlinearity of RSMs, but they can be applied differently because of the different characteristics. RSM flux model I has a simple process introducing the energy conservation rule, which holds only the simple prototype functions. On the other hand, RSM flux model II possesses a more flexible prototype function structure, which still follows the reciprocity theorem. By consisting of not only the reused self-axis functions but also the modified Gaussian functions, the cross-saturation effect of RSMs over the whole operation range can be modeled adequately.

V. IPMSM FLUX LINKAGE PROTOTYPE FUNCTION

Now, analytical flux linkage prototype functions for IPMSMs are presented. Due to the existence of the PM flux linkage, an offset is introduced and the asymmetry of the flux linkages increases, which make the development of analytical prototype functions for the whole operation range more difficult. The developed RSM model II is adopted but further modified to accommodate the IPMSMs difficulties.

A. ANALYTICAL PROTOTYPE FUNCTION

In [23], the same approach presented with the RSM model I has been applied to PM-assisted RSM (PMaRSM). It is stated that the flux linkages must be modeled separately into two parts when the d-axis (aligned to PM flux) current is positive or negative. Compared to PMaRSMs, IPMSMs have higher PM flux linkage values. Its cross-coupling flux linkage curves change throughout the whole current domain, especially when i_s^d is negative. As shown in Fig. 5(b), the part of the zero locus $\mathbb{L}_\mathrm{s}^{dq}(L=0)$ parallel to the vertical q-axis converges gradually to a constant negative i_s^d-value of -0.53p.u. This prevents the RSM model I from being applicable for IPMSMs, because a rectangular region must be defined for deriving the varying coenergy values. Therefore, for IPMSMs, the flux linkage surfaces must be divided into at least *four* regions and for each region separate prototype functions must be derived, which is complicated and impractical.

The RSM flux model II possesses a greater flexibility; therefore, it is chosen and extended for IPMSMs in the following. As shown in Fig. 5(b), different saturation effects on the left and right sides of the vertical zero locus $\mathbb{L}_\mathrm{s}^{dq}(L=0)$ can be observed. The values of the differential inductance L_s^{dq} on the left side are smaller than those on the right side. Thus, due to this "twisted" characteristic of the zero locus $\mathbb{L}_\mathrm{s}^{dq}(L=0)$ and different saturation extents between both sides, the flux linkage surfaces of IPMSMs are cut along the vertical (d-) direction of the zero locus $\mathbb{L}_\mathrm{s}^{dq}(L=0)$ into *two* parts only and modeled separately (see regions 1 & 2 in Fig. 10).

In the first region (reg1), i.e. Region 1 in Fig. 10, which is located in the right part of the zero locus $\mathbb{L}_\mathrm{s}^{dq}(L=0)$, the IPMSM flux linkages can be approximated by

$$\widehat{\psi}_{\mathrm{s,reg1}}^{d}(i_\mathrm{s}^d, i_\mathrm{s}^q) = \widehat{\psi}_{\mathrm{s,self1}}^{d}(i_\mathrm{s}^d) - \widehat{\psi}_{\mathrm{s,cross1}}^{d}(i_\mathrm{s}^d, i_\mathrm{s}^q) \tag{40}$$

and

$$\widehat{\psi}_{\mathrm{s,reg1}}^{q}(i_\mathrm{s}^d, i_\mathrm{s}^q) = \widehat{\psi}_{\mathrm{s,self1}}^{q}(i_\mathrm{s}^q) - \widehat{\psi}_{\mathrm{s,cross1}}^{q}(i_\mathrm{s}^d, i_\mathrm{s}^q), \tag{41}$$

where $\widehat{\psi}_{\mathrm{s,self1}}^{d}$ & $\widehat{\psi}_{\mathrm{s,self1}}^{q}$ and $\widehat{\psi}_{\mathrm{s,cross1}}^{d}$ & $\widehat{\psi}_{\mathrm{s,cross1}}^{q}$ are the self-axis and cross-coupling saturation terms in the first region. Note that the prototype subfunctions $\widehat{\psi}_{\mathrm{s,cross1}}^{d}$ and $\widehat{\psi}_{\mathrm{s,cross1}}^{q}$ have a similar structure as those defined in (32) and (33).

The IPMSM self-axis flux linkage curves for both axes are shown in Fig. 3(c) and 3(d). Their similarity in the saturation trends with those of RSMs is obvious and motivates for the reuse and adaption of the RSM prototype functions. For

$$\widehat{\psi}_{\mathrm{s,self1}}^{d}(i_\mathrm{s}^d) = a_{\mathrm{d1}} \tanh\Big(a_{\mathrm{d2}}(i_\mathrm{s}^d - a_{\mathrm{d3}})\Big) \tag{42}$$

the linear function in (13) is replaced by a horizontal shift by a_{d3} in the hyperbolic tangent function to take additionally the PM flux linkage (offset) into account. For

$$\widehat{\psi}_{\mathrm{s,self1}}^{q}(i_\mathrm{s}^q) = a_{\mathrm{q1}} \tanh\left(a_{\mathrm{q2}} i_\mathrm{s}^q\right) + a_{\mathrm{q3}} i_\mathrm{s}^q, \tag{43}$$

which means $\widehat{\psi}_\mathrm{s}^{q}(i_\mathrm{s}^d = I_{\mathrm{zl}}, i_\mathrm{s}^q)$, where I_{zl} changes along the zero locus $\mathbb{L}_\mathrm{s}^{dq}(L=0)$ (recall Fig. 5(b) and Fig. 10). (14) can be reused directly due to the symmetric rotor structure along the q-axis.

For the IPMSM cross-saturation effects, as shown in Fig. 3(e), 3(f) and 4, the modified Gaussian function prototypes in (34) and (35) can be reused as well. However, the maximum or minimum values of ψ_s^q over i_s^d occur at negative i_s^d-values and move gradually to constant asymptote, which can be seen in Fig. 3(f) and Fig. 5(b). Therefore, in $\widehat{\psi}_{\mathrm{s,cross1}}^{q}$, $F_1, \ldots, F_\mathrm{n}$ describe how i_s^d affects ψ_s^q and must be shifted horizontally along the d-axis. Due to less nonlinearities compared to RSMs, the cross-coupling prototype functions can be built with $n = 2$ and are given by

$$F_1(i_\mathrm{s}^d) = 1 - e^{-\left(a_{\mathrm{d4}}(i_\mathrm{s}^d - a_{\mathrm{d5}})\right)^2}, F_2(i_\mathrm{s}^d) = 1 - e^{-\left(a_{\mathrm{d6}}(i_\mathrm{s}^d - a_{\mathrm{d7}})\right)^2} \tag{44}$$

and

$$G_1(i_\mathrm{s}^q) = 1 - e^{-(a_{\mathrm{q4}} i_\mathrm{s}^q)^2}, G_2(i_\mathrm{s}^q) = 1 - e^{-(a_{\mathrm{q5}} i_\mathrm{s}^q)^2}, \tag{45}$$

where a_{d5} and a_{d7} shift the functions horizontally and the other parameters affect the cross-coupling saturation. The differential terms F_1', F_2' and G_1', G_2' can be easily derived.

In the second region (reg2), i.e. Region 2 in Fig. 10, which is located in the left part of the zero locus $\mathbb{L}_\mathrm{s}^{dq}(L = 0)$, the flux linkages can be modeled by

$$\widehat{\psi}_{\mathrm{s,reg2}}^{d}(i_\mathrm{s}^d, i_\mathrm{s}^q) = \widehat{\psi}_{\mathrm{s,self2}}^{d}(i_\mathrm{s}^d) - \widehat{\psi}_{\mathrm{s,cross2}}^{d}(i_\mathrm{s}^d, i_\mathrm{s}^q) \tag{46}$$

$$\widehat{\psi}_{\mathrm{s,reg2}}^{q}(i_\mathrm{s}^d, i_\mathrm{s}^q) = \widehat{\psi}_{\mathrm{s,self1}}^{q}(i_\mathrm{s}^q) - \widehat{\psi}_{\mathrm{s,cross2}}^{q}(i_\mathrm{s}^d, i_\mathrm{s}^q) \tag{47}$$

which are composed of self-axis $\widehat{\psi}_{\mathrm{s,self2}}^{d}$ & $\widehat{\psi}_{\mathrm{s,self1}}^{q}$ and cross-coupling saturation $\widehat{\psi}_{\mathrm{s,cross2}}^{d}$ & $\widehat{\psi}_{\mathrm{s,cross2}}^{q}$ terms. Both, $\widehat{\psi}_{\mathrm{s,cross2}}^{d}$ and $\widehat{\psi}_{\mathrm{s,cross2}}^{q}$ possess the identical structure as those in (32) and (33).

Due to the shared contour lines along the zero locus $\mathbb{L}_\mathrm{s}^{dq}(L=0)$, $\widehat{\psi}_{\mathrm{s,self1}}^{q}$ from the first region can be reused in (47). In contrast to that, $\widehat{\psi}_{\mathrm{s,self2}}^{d}$ must be modeled separately in the second region. Instead of shifting the function as in (42), an offset is added in order to achieve a better fitting performance, because ψ_s^d does only saturate slowly for negative i_s^d (almost linear behavior). Hence, it is approximated by

$$\widehat{\psi}_{\mathrm{s,self2}}^{d}(i_\mathrm{s}^d) = a_{\mathrm{d8}} \tanh\left(a_{\mathrm{d9}} i_\mathrm{s}^d\right) + a_{\mathrm{d10}} \tag{48}$$

where a_{d8} and a_{d9} represent the gradual saturation and allow for a smooth transition between the saturated regions, and a_{d10} represents the PM flux linkage offset in d-direction. By following the same ideas as introduced in (44) and (45), the cross-saturation terms (for $n = 2$) can be modeled as

$$F_3(i_\mathrm{s}^d) = 1 - e^{-\left(a_{\mathrm{d11}}(i_\mathrm{s}^d - a_{\mathrm{d5}})\right)^2}, F_4(i_\mathrm{s}^d) = 1 - e^{-\left(a_{\mathrm{d12}}(i_\mathrm{s}^d - a_{\mathrm{d7}})\right)^2} \tag{49}$$

and

$$G_3(i_\mathrm{s}^q) = 1 - e^{-(a_{\mathrm{q6}} i_\mathrm{s}^q)^2}, G_4(i_\mathrm{s}^q) = 1 - e^{-(a_{\mathrm{q7}} i_\mathrm{s}^q)^2} \tag{50}$$

where $a_{\mathrm{d11}}, a_{\mathrm{d12}}$ and $a_{\mathrm{q6}}, a_{\mathrm{q7}}$ control the opening widths of the Gaussian functions. The horizontal shifts a_{d5} and a_{d7} in

(44) are reused here, as the maximum or minimum cross-coupling flux linkages occur always at the shared contour lines between the first and second region. After computing the derivative terms of (49) and (50), all the required prototype functions for the IPMSM flux linkage approximation are found.

B. FITTING PROCEDURE

Due to the asymmetry of the IPMSM flux linkage surfaces, its analytical prototype functions are modeled by two separate parts. Therefore, the procedure, which is similar for the RSM flux model II, is invoked and adjusted for the fitting process of self- and cross-coupling saturation terms in both regions. For the self-saturation terms in (42), (43) and (48), the corresponding parameters must be found by solving the following minimization problems

$$\min_{a_{\mathrm{d1}},a_{\mathrm{d2}},a_{\mathrm{d3}}} \sum_{j=1}^{m} \left[\psi_{\mathrm{s}}^{d}(i_{\mathrm{s},j}^{d},0) - \widehat{\psi}_{\mathrm{s,self1}}^{d}(i_{\mathrm{s},j}^{d},a_{\mathrm{d1}},a_{\mathrm{d2}},a_{\mathrm{d3}}) \right]^2, \tag{51}$$

$$\min_{a_{\mathrm{q1}},a_{\mathrm{q2}},a_{\mathrm{q3}}} \sum_{k=1}^{n} \left[\psi_{\mathrm{s}}^{q}(I_{\mathrm{zl}},i_{\mathrm{s},k}^{q}) - \widehat{\psi}_{\mathrm{s,self1}}^{q}(i_{\mathrm{s},k}^{q},a_{\mathrm{q1}},a_{\mathrm{q2}},a_{\mathrm{q3}}) \right]^2 \tag{52}$$

and

$$\min_{a_{\mathrm{d8}},a_{\mathrm{d9}},a_{\mathrm{d10}}} \sum_{j=1}^{m} \left[\psi_{\mathrm{s}}^{d}(i_{\mathrm{s},j}^{d},0) - \widehat{\psi}_{\mathrm{s,self2}}^{d}(i_{\mathrm{s},j}^{d},a_{\mathrm{d8}},a_{\mathrm{d9}},a_{\mathrm{d10}}) \right]^2. \tag{53}$$

Afterwards, the reference samples of the cross-coupling saturation surfaces can be obtained according to (40), (41), (46) and (47). For both regions, the cross-coupling saturation terms with shared parameters can be fitted by minimizing

$$\min_{\boldsymbol{a}_{\mathrm{dq1}}} \sum_{j=1}^{m}\sum_{k=1}^{n} \left[\psi_{\mathrm{s,cross1}}^{d}(i_{\mathrm{s},j}^{d},i_{\mathrm{s},k}^{q}) - \widehat{\psi}_{\mathrm{s,cross1}}^{d}(i_{\mathrm{s},j}^{d},i_{\mathrm{s},k}^{q},\boldsymbol{a}_{\mathrm{dq1}}) \right]^2 + \left[\psi_{\mathrm{s,cross1}}^{q}(i_{\mathrm{s},j}^{d},i_{\mathrm{s},k}^{q}) - \widehat{\psi}_{\mathrm{s,cross1}}^{q}(i_{\mathrm{s},j}^{d},i_{\mathrm{s},k}^{q},\boldsymbol{a}_{\mathrm{dq1}}) \right]^2 \tag{54}$$

and

$$\min_{\boldsymbol{a}_{\mathrm{dq2}}} \sum_{j=1}^{m}\sum_{k=1}^{n} \left[\psi_{\mathrm{s,cross2}}^{d}(i_{\mathrm{s},j}^{d},i_{\mathrm{s},k}^{q}) - \widehat{\psi}_{\mathrm{s,cross2}}^{d}(i_{\mathrm{s},j}^{d},i_{\mathrm{s},k}^{q},\boldsymbol{a}_{\mathrm{dq2}}) \right]^2 + \left[\psi_{\mathrm{s,cross2}}^{q}(i_{\mathrm{s},j}^{d},i_{\mathrm{s},k}^{q}) - \widehat{\psi}_{\mathrm{s,cross2}}^{q}(i_{\mathrm{s},j}^{d},i_{\mathrm{s},k}^{q},\boldsymbol{a}_{\mathrm{dq2}}) \right]^2 \tag{55}$$

where $\psi_{\mathrm{s,cross1}}^{d}$ & $\psi_{\mathrm{s,cross1}}^{q}$ and $\psi_{\mathrm{s,cross2}}^{d}$ & $\psi_{\mathrm{s,cross2}}^{q}$ are the references of cross-coupling flux surfaces in the first and second region. The parameter vectors

$$\boldsymbol{a}_{\mathrm{dq1}} = (a_{\mathrm{d4}}, a_{\mathrm{d5}}, a_{\mathrm{d6}}, a_{\mathrm{d7}}, a_{\mathrm{q4}}, a_{\mathrm{q5}}, k_1, k_2)^{\top}$$

and

$$\boldsymbol{a}_{\mathrm{dq2}} = (a_{\mathrm{d5}}, a_{\mathrm{d7}}, a_{\mathrm{d11}}, a_{\mathrm{d12}}, a_{\mathrm{q6}}, a_{\mathrm{q7}}, k_3, k_4)^{\top}$$

comprise all fitting parameters of the cross-coupling saturation terms.

With the obtained parameters above using as initial values, the entire analytical functions in (40), (41), (46) and (47) are fitted now at once in the final fitting step. Consequently, not only the approximation errors due to the separate fitting in the previous steps can be compensated for, but also the shared parameters $a_{\mathrm{q1}}, a_{\mathrm{q2}}, a_{\mathrm{q3}}$ as in (43) and $a_{\mathrm{d5}}, a_{\mathrm{d7}}$ as in (44) and (49) which are used in both regions can be fitted together to achieve globally optimal values. The final IPMSM flux linkage prototype function parameter set can be obtained by minimizing the following optimization problem

$$\begin{aligned}\min_{\boldsymbol{a}_{\mathrm{dq}}} &\sum_{j=1}^{m}\sum_{k=1}^{n} \left[\psi_{\mathrm{s,reg1}}^{d}(i_{\mathrm{s},j}^{d},i_{\mathrm{s},k}^{q}) - \widehat{\psi}_{\mathrm{s,reg1}}^{d}(i_{\mathrm{s},j}^{d},i_{\mathrm{s},k}^{q},\boldsymbol{a}_{\mathrm{dq}}) \right]^2 \\ &+ \left[\psi_{\mathrm{s,reg1}}^{q}(i_{\mathrm{s},j}^{d},i_{\mathrm{s},k}^{q}) - \widehat{\psi}_{\mathrm{s,reg1}}^{q}(i_{\mathrm{s},j}^{d},i_{\mathrm{s},k}^{q},\boldsymbol{a}_{\mathrm{dq}}) \right]^2 \\ &+ \sum_{f=1}^{x}\sum_{h=1}^{y} \left[\psi_{\mathrm{s,reg2}}^{d}(i_{\mathrm{s},f}^{d},i_{\mathrm{s},h}^{q}) - \widehat{\psi}_{\mathrm{s,reg2}}^{d}(i_{\mathrm{s},f}^{d},i_{\mathrm{s},h}^{q},\boldsymbol{a}_{\mathrm{dq}}) \right]^2 \\ &+ \left[\psi_{\mathrm{s,reg2}}^{q}(i_{\mathrm{s},f}^{d},i_{\mathrm{s},h}^{q}) - \widehat{\psi}_{\mathrm{s,reg2}}^{q}(i_{\mathrm{s},f}^{d},i_{\mathrm{s},h}^{q},\boldsymbol{a}_{\mathrm{dq}}) \right]^2 \end{aligned} \tag{56}$$

where $\psi_{\mathrm{s,reg1}}^{d}$ & $\psi_{\mathrm{s,reg1}}^{q}$ and $\psi_{\mathrm{s,reg2}}^{d}$ & $\psi_{\mathrm{s,reg2}}^{q}$ are the reference flux linkages in the first and second region and $(i_{\mathrm{s},j}^{d}, i_{\mathrm{s},k}^{q})$ are the j-th and k-th current data points of the first region, and $(i_{\mathrm{s},f}^{d}, i_{\mathrm{s},h}^{q})$ are the f-th and h-th current data points of the second region. The overall parameter vector

$$\boldsymbol{a}_{\mathrm{dq}} = (a_{\mathrm{d1}}, \ldots, a_{\mathrm{d12}}, a_{\mathrm{q1}}, \ldots, a_{\mathrm{q7}}, k_1, \ldots, k_4)^{\top}$$

consists of 23 fitting parameters in total for d- and q-axis flux linkage prototype functions.

C. APPROXIMATION RESULTS

In order to evaluate the developed IPMSM flux linkage prototype functions, the real flux maps of a 3.4 kW IPMSM are employed as reference. Its parameters are listed in Table 2 in the appendix. Its real flux linkages are used to fit the analytical flux linkage prototype functions in (40), (41), (46) and (47) and to obtain the optimal parameters $a_{\mathrm{d1}}, \ldots, a_{\mathrm{d12}}$, $a_{\mathrm{q1}}, \ldots, a_{\mathrm{q7}}$ and $k_1, \ldots, k_4$. These fitted parameters are collected in Table 3 in the appendix. Due to the existence of a permanent magnet, the IPMSM flux linkage maps are separated into the two regions (Regions 1 & 2 in Fig. 10) of the zero locus $\mathbb{L}_{\mathrm{s}}^{dq}(L=0)$ and modeled separately.

The approximated IPMSM d-axis flux linkage $\widehat{\psi}_{\mathrm{s}}^{d}$ and q-axis flux linkage $\widehat{\psi}_{\mathrm{s}}^{q}$ are shown in Fig. 10(a) and 10(b), respectively. Its smooth surfaces confirm continuity and differentiability of the proposed prototype functions. Instead of showing the surfaces of Regions 1 & 2 separately, they are merged to form the entire flux linkage approximations $\widehat{\psi}_{\mathrm{s}}^{d}$ and $\widehat{\psi}_{\mathrm{s}}^{q}$, respectively. The shared boundaries (contour lines) of the zero locus $\mathbb{L}_{\mathrm{s}}^{dq}(L=0)$ [——] between first and second region are shown. Furthermore, the approximated IPMSM flux linkages [- - -, - - -, - - -] plotted in Fig. 3(c), 3(d), 3(e) & 3(f) and Fig. 4 confirm the very good fitting accuracy of the self-axis and cross-coupling saturation terms.

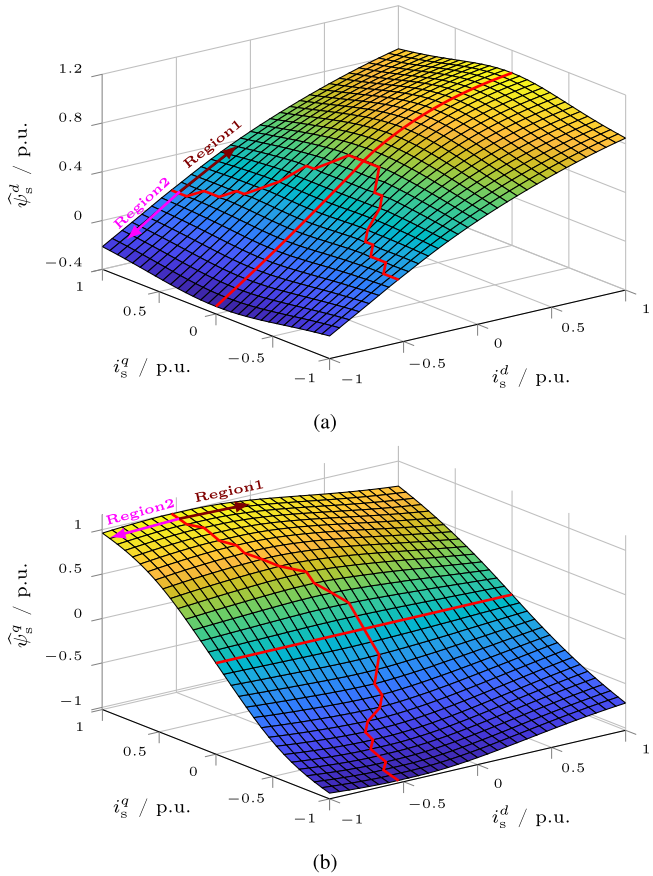

FIGURE 10. Approximation results of the proposed analytical flux linkage prototype functions (40), (41), (46) and (47): (a) fitted *d*-axis flux linkages $\widehat{\psi}_s^d$; (b) fitted *q*-axis flux linkages $\widehat{\psi}_s^q$; zero locus $\mathbb{L}_s^{dq}(L=0)$ [——] is indicated.

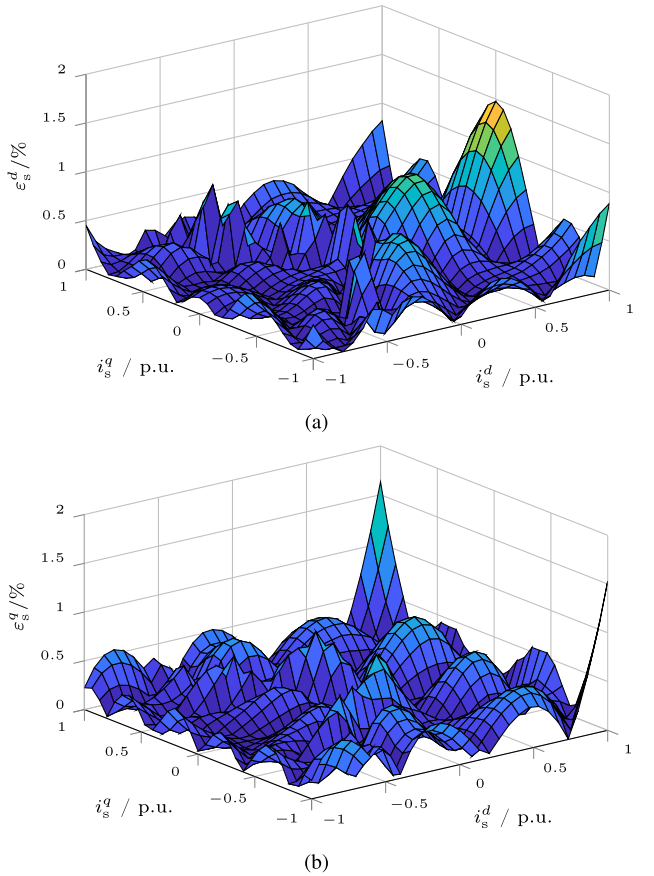

FIGURE 11. Approximation errors of the proposed analytical flux linkage prototype functions (40), (41), (46) and (47) compared to the real flux maps: (a) normalized *d*-axis error ε_s^d; (b) normalized *q*-axis error ε_s^q.

The normalized errors ε_s^d and ε_s^q are shown in Fig. 11(a) and 11(b), respectively. In both error plots, a very good fitting accuracy with less than 2% approximation errors over the whole current operation range is achieved. Therefore, the effectiveness of the developed analytical flux linkage prototype functions for IPMSMs with proper separation is confirmed.

The differential inductances L_s^d, L_s^q, L_s^{dq} computed by the real IPMSM flux linkages are presented in Fig. 12(a), 12(b) and 12(c), respectively. In Fig. 12(d), 12(e) and 12(f), the approximated differential inductances $\widehat{L}_s^d$, $\widehat{L}_s^q$ and $\widehat{L}_s^{dq}$, obtained by analytical differentiation of the flux linkage prototype functions in (40), (41), (46) and (47), are shown. For $\widehat{L}_s^d$, bumpy parts in the map near the shared boundary can be seen due to the slight different values at the border of the two regions. In general, with higher flux linkage approximation accuracy, the approximated differential inductances of IPMSM match the real differential inductances much better than those of the RSM approximation.

VI. DISCUSSION AND COMPARISON WITH OTHER STATE-OF-THE-ART APPROXIMATION METHODS

This section discusses and compares important aspects of prototype functions used in the literature in order to show the potential of the developed flux linkage prototype functions. In Table 1, a comparison of key characteristics/properties of different prototype functions is shown. The checkmark (✓) indicates that the characteristic/property is covered, whereas the cross (×) indicates that the characteristic/property is *not* covered in the respective publication.

1) **Flux linkage maps:** Current maps $\boldsymbol{i}_s^{dq}(\boldsymbol{\psi}_s^{dq})$, which use the flux linkages as state variables, are more common [12], [14], [15] than flux linkage maps. The flux-to-current curves saturate similarly as a polynomial with odd power number. This property of the current maps motivates for the very common utilization of polynomials as prototype functions. However, the machine's stator currents are measured in almost every application. Therefore, flux linkage maps $\boldsymbol{\psi}_s^{dq}(\boldsymbol{i}_s^{dq})$ are more practical. In both [11], [16], one-dimensional (1D) flux linkage curves (lines), i.e. $\psi_s^d(i_s^d)$ and $\psi_s^q(i_s^q)$, are developed. Therefore, the two-dimensional (2D) flux linkage maps (surfaces) can not be represented by *one* function each. They can only be approximated line by line for different but constant cross-coupling currents (which requires LUT-like interpolation methods). In contrast, 2D flux linkage prototype functions, which dependent on both *d*- and *q*-axis currents, are developed in [13], [18].

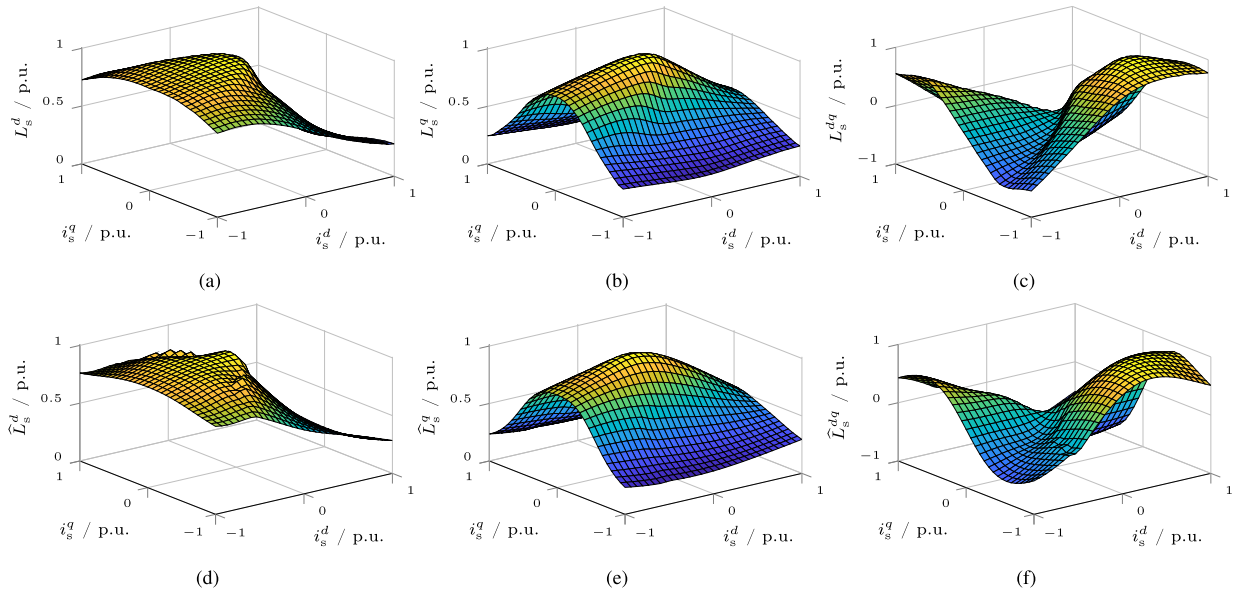

FIGURE 12. Differential inductances of the considered IPMSM: (a) real *d*-axis differential inductance L_s^d; (b) real *q*-axis differential inductance L_s^q; (c) real cross-coupling differential inductance L_s^{dq}; (d) approximated *d*-axis differential inductance $\widehat{L}_s^d$ derived from (40), (41), (46) and (47); (e) approximated *q*-axis differential inductance $\widehat{L}_s^q$ derived from (40), (41), (46) and (47); (f) approximated cross-coupling differential inductance $\widehat{L}_s^{dq}$ derived from (40), (41), (46) and (47).

TABLE 1. Comparison of Key Characteristics/Properties of Different Prototype Functions Found in Literature

Method	Flux linkage maps	Energy conservation	Differen-tiability	Over-range capability	Extensibility
Current bivariate polynomial [12]	×	✓	×	✓	✓
Modified power function [14], [15]	×	✓	×	✓	×
High-order polynomial [11]	× (1D)	×	(✓)	×	✓
Flux bivariate polynomial [13]	✓	×	✓	×	×
Piece-wise function [16]	× (1D)	×	×	✓	×
ANN training [18]	✓	×	✓	×	✓
Prototypes in this paper	✓	✓	✓	✓	✓

Rather simple bivariate quadratic polynomial functions are utilized to approximate the flux linkages of PMSMs in [13]; however, due to their low equation order, the functions require a separate fitting for each of the four quadrants and are not applicable for highly nonlinear RSMs. Artificial neural networks (ANNs) [18] result in the most complex, recursively defined mathematical expressions, which cause a high computational burden similar to LUT-based methods. Compared to the above-mentioned methods, the proposed flux linkage prototype functions can easily be applied e.g. (i) to compensate for machine nonlinearities, (ii) to implement nonlinear/adaptive current controllers [4] or (iii) optimal feedforward torque control [5].

2) **Energy conservation:** With the consideration of energy conservation (reciprocity rule), the proposed prototype functions can directly represent physical properties and reduce the number of required parameters for fitting by sharing common parameters along both axes. In Table 1, it can be seen that only current prototype functions consider the reciprocity rule. In contrast to that, other available flux linkage prototype functions, such ANNs [18] or flux bivariate polynomials [13], do not obey it and thus require a larger number of parameters to approximate the entire flux linkage maps. The 7th order polynomials proposed in [11] allow to approximate the self-axis flux linkage curves of SPMSMs (which possess an almost linear magnetic behavior without saturation) but different cross-coupling current constants must be found to achieve an acceptable fitting accuracy over the whole current range. Nevertheless, a two-dimensional function is not obtained and, therefore, the reciprocity rule is violated.

3) **Differentiability (with respect to the self-axis and cross-coupling currents)**: To simplify the fitting process, prototype functions often approximate the non-saturated regions and the saturated regions separately and/or contain non-differentiable absolute value

functions of the currents [14]–[16] and, therefore, are not globally continuously differentiable. Moreover, all approaches which approximate the currents as functions of the flux linkages (current maps) [12], [14], [15] are not differentiable with respect to the currents. Furthermore, the flux linkage prototype functions proposed in [11], [16] are composed of several segments with different cross-coupling current sets. Besides, single-variant polynomials as in [11] can only be seen as quasi-differentiable (with respect to the self-axis current), differential cross-coupling inductances can not be derived as an analytical differentiation is not feasible (with respect to the cross-coupling current). Consequently, discontinuous functions are obtained which do not allow to analytically derive or compute (continuously) differential inductances. ANNs [18] (with Gaussion like activation functions) or flux bivariate polynomials [13] are clearly continuously differentiable. However, both do not allow to represent the physically meaningful differential inductances properly as the reciprocity rule does not hold. The proposed flux linkage prototype functions are globally continuously differentiable due to their physics-based design.

4) **Over-range capability:** The fitting with power functions [14], [15], polynomials [11]–[13], piece-wise continuous functions [16] or ANNs [18] usually requires many parameters to minimize the approximation error globally. Nevertheless, the resulting and parametrized prototype functions may produce severe inaccuracies or even oscillations when the input currents are outside of the range of the used fitting samples or training data. Conversely, if the proposed prototype functions are designed properly, these problems will not arise.
5) **Extensibility:** The proposed physically motivated prototype functions are capable of approximating flux linkages of all types of synchronous machines as their generic design is based on physical and intrinsic magnetic properties of real flux linkages. Power functions [14], [15], polynomials [11]–[13], piece-wise continuous functions [16] or ANNs [18] cannot cover different machine types as easily as many redundant parameters must be fitted. For example, in [12], current bivariate polynomials must be extended by a constant to cover the offset effect due to permanent magnets in IPMSMs. However, only two quadrants with positive i_s^d are considered; hence, not the full operation range is covered. The available methods are not as practical as the proposed generic function prototypes when the flux linkages of different SMs should be approximated with one type of prototype functions.

In summary, in contrast to the proposed prototype functions, the existing flux linkage (or current) prototype functions are often expressed in complicated forms and lack of generic expressions to cover all relevant physical properties of real flux linkages (see above). To overcome this bottleneck, the physically motivated and analytical flux linkage prototype functions are developed to be capable of approximating the flux linkages of any SM in an intrinsic and generic form. The proposed continuously differentiable prototype functions can represent typical magnetic saturation effects very well. Moreover, the differential inductances can easily be computed by computing the respective partial derivatives analytically. Finally, thanks to the consideration of energy conservation, the developed prototype functions have physical meaning and make redundant parameters obsolete.

VII. CONCLUSION

This paper has presented analytical flux linkage prototype functions which allow to generically approximate the nonlinear flux linkages of RSMs and IPMSMs. Due to their continuity and differentiability over the whole current range, the analytical prototype functions are very beneficial to ease the analysis of machine characteristics and to use them in real-world applications; such as advanced nonlinear control, operation management or self-commissioning. Three flux linkage prototype functions are presented; all obey the energy conservation rule. First, a prototype function was proposed for the modeling of RSM flux linkages. It has a simple and intuitive structure and only a few parameters need to be fitted. Then, a second RSM flux linkage prototype function was developed based on the first approach in order to provide a higher flexibility and to achieve a better fitting accuracy. The number of cross-saturation terms can be chosen arbitrarily according to the requirements induced by different applications. At the end, an analytical flux linkage prototype function for IPMSMs was developed based on the second RSM flux model. Due to the asymmetric saturation effects in IPMSMs, the flux linkage surfaces must (i) be separated into two regions along a curved line in the d-direction of the zero locus of the differential inductances and (ii) modeled separately. The parameters of the prototype function of both regions are obtained by an effective fitting process. Finally, all three flux linkage prototype functions were validated against real flux linkages of an RSM and an IPMSM showing very high approximation accuracies.

The proposed flux linkage prototype functions are: (i) physically motivated and designed to describe the self-axis and cross-coupling saturation effects; (ii) continuously differentiable throughout the whole operation range; (iii) avoiding the need of many and redundant parameters; and (iv) applicable for both RSMs and IPMSMs. These advantages can facilitate the implementation of more sophisticated control algorithms in the real-time system. Future work will focus on the application of the proposed flux linkage prototype functions in nonlinear/adaptive current control and optimal feedforward torque control (efficiency improvement and operation management) of different and highly nonlinear SMs.

APPENDIX A MACHINE AND FITTED PARAMETERS

The key parameters of the employed machines are listed in Table 2. Maximum values of $\widehat{i}_{\mathrm{s,max}}$, $\psi_{\mathrm{s,max}}^d$, $\psi_{\mathrm{s,max}}^q$, $L_{\mathrm{s,max}}^d$,

TABLE 2. Key Parameters of Employed RSM and IPMSM

Parameter	Symbol	RSM	IPMSM
Rated power	P_{R}	9.6 kW	3.4 kW
Rated speed	$\omega_{\mathrm{m,R}}$	157.1 rad/s	576.0 rad/s
Rated torque	$m_{\mathrm{m,R}}$	61 N m	6 N m
Rated current	$\widehat{i}_{\mathrm{s,R}}$	29.7 A	35.0 A
Rated voltage	$\widehat{u}_{\mathrm{s,R}}$	326.6 V	130.0 V
Stator resistance	R_{s}	0.4 Ω	0.2 Ω
Maximum current	$\widehat{i}_{\mathrm{s,max}}$	38.0 A	45.0 A
Maximum d-axis flux linkage	$\psi^{d}_{\mathrm{s,max}}$	1.06 Wb	63.6 mWb
Maximum q-axis flux linkage	$\psi^{q}_{\mathrm{s,max}}$	0.48 Wb	56.4 mWb
Maximum d-axis differential inductance	$L^{d}_{\mathrm{s,max}}$	115.7 mH	1.34 mH
Maximum q-axis differential inductance	$L^{q}_{\mathrm{s,max}}$	46.9 mH	2.13 mH
Maximum cross-coupling differential inductance	$L^{dq}_{\mathrm{s,max}}$	8.1 mH	0.38 mH

TABLE 3. Fitted Parameters of the Proposed Flux Linkage Prototype Functions for the Employed RSM and IPMSM

Model	Parameters
RSM I	$a_{\mathrm{d1}} = 0.943, a_{\mathrm{d2}} = 0.138, a_{\mathrm{d3}} = 0.003,$ $a_{\mathrm{d4}} = 0.869, a_{\mathrm{d5}} = 0.092, a_{\mathrm{d6}} = 0.003,$ $a_{\mathrm{q1}} = 0.096, a_{\mathrm{q2}} = 0.403, a_{\mathrm{q3}} = 0.010,$ $a_{\mathrm{q4}} = 0.031, a_{\mathrm{q5}} = 0.105, a_{\mathrm{q6}} = 0.008$
RSM II	$a_{\mathrm{d1}} = 0.943, a_{\mathrm{d2}} = 0.138, a_{\mathrm{d3}} = 0.003,$ $a_{\mathrm{d4}} = 0.029, a_{\mathrm{d5}} = 0.064, a_{\mathrm{d6}} = 0.223, a_{\mathrm{d7}} = 0.101,$ $a_{\mathrm{q1}} = 0.098, a_{\mathrm{q2}} = 0.464, a_{\mathrm{q3}} = 0.010,$ $a_{\mathrm{q4}} = 0.008, a_{\mathrm{q5}} = 0.084, a_{\mathrm{q6}} = 0.227, a_{\mathrm{q7}} = 0.020,$ $k_1 = 33.032, k_2 = 0.581, k_3 = 0.202, k_4 = 3.567$
IPMSM	$a_{\mathrm{d1}} = 0.070, a_{\mathrm{d2}} = 0.023, a_{\mathrm{d3}} = -25.404,$ $a_{\mathrm{d4}} = 0.021, a_{\mathrm{d5}} = -21.080, a_{\mathrm{d6}} = 0.012,$ $a_{\mathrm{d7}} = -0.938, a_{\mathrm{d8}} = 0.157, a_{\mathrm{d9}} = 0.009,$ $a_{\mathrm{d10}} = 0.037, a_{\mathrm{d11}} = 0.020, a_{\mathrm{d12}} = 0.048,$ $a_{\mathrm{q1}} = 0.048, a_{\mathrm{q2}} = 0.042, a_{\mathrm{q3}} = 2.285e\text{-}4,$ $a_{\mathrm{q4}} = 0.018, a_{\mathrm{q5}} = 0.039, a_{\mathrm{q6}} = 0.026, a_{\mathrm{q7}} = 0.052,$ $k_1 = 1.156, k_2 = 0.597, k_3 = 0.680, k_4 = 0.066$

$L^{q}_{\mathrm{s,max}}$ and $L^{dq}_{\mathrm{s,max}}$ are used as the base values for the normalization to obtain the per unit (p.u.) representation. Finally, the fitted parameters of the proposed flux linkage prototype functions are collected in Table 3.

REFERENCES

[1] H. Murakami, Y. Honda, H. Kiriyama, S. Morimoto, and Y. Takeda, "The performance comparison of SPMSM, IPMSM and SynRM in use as air-conditioning compressor," in *Proc. IEEE Ind. Appl. Conf. 34th IAS Annu. Meeting*, 1999, pp. 840–845.

[2] A. Vagati, M. Pastorelli, F. Scapino, and G. Franceschini, "Impact of cross saturation in synchronous reluctance motors of the transverse-laminated type," *IEEE Trans. Ind. Appl.*, vol. 36, no. 4, pp. 1039–1046, Jul./Aug. 2000.

[3] B. Stumberger, G. Stumberger, D. Dolinar, A. Hamler, and M. Trlep, "Evaluation of saturation and cross-magnetization effects in interior permanent-magnet synchronous motor," *IEEE Trans. Ind. Appl.*, vol. 39, no. 5, pp. 1264–1271, Sep./Oct. 2003.

[4] C. M. Hackl, M. J. Kamper, J. Kullick, and J. Mitchell, "Current control of reluctance synchronous machines with online adjustment of the controller parameters," in *Proc. IEEE Int. Symp. Ind. Electron.*, 2016, pp. 153–160.

[5] H. Eldeeb, C. M. Hackl, L. Horlbeck, and J. Kullick, "A unified theory for optimal feedforward torque control of anisotropic synchronous machines," *Int. J. Control*, vol. 91, no. 10, pp. 2273–2302, 2018.

[6] C. Hackl, J. Kullick, and N. Monzen, "Generic loss minimization for nonlinear synchronous machines by analytical computation of optimal reference currents considering copper and iron losses," in *Proc. 22nd IEEE Int. Conf. Ind. Technol.*, 2021, pp. 1348–1355.

[7] S. Wendel, P. Karamanakos, A. Dietz, and R. Kennel, "Flux linkage-based model predictive current control for nonlinear PMSM drives," in *Proc. IEEE 46th Annu. Conf. IEEE Ind. Electron. Soc.*, 2020, pp. 3051–3056.

[8] D. Mingardi, M. Morandin, S. Bolognani, and N. Bianchi, "On the proprieties of the differential cross-saturation inductance in synchronous machines," *IEEE Trans. Ind. Appl.*, vol. 53, no. 2, pp. 991–1000, Mar./Apr. 2017.

[9] E. Armando, R. I. Bojoi, P. Guglielmi, G. Pellegrino, and M. Pastorelli, "Experimental identification of the magnetic model of synchronous machines," *IEEE Trans. Ind. Appl.*, vol. 49, no. 5, pp. 2116–2125, Sept./Oct. 2013.

[10] S. A. Odhano, P. Pescetto, H. A. A. Awan, M. Hinkkanen, G. Pellegrino, and R. Bojoi, "Parameter identification and self-commissioning in AC motor drives: A technology status review," *IEEE Trans. Power Electron.*, vol. 34, no. 4, pp. 3603–3614, Apr. 2019.

[11] M. Seilmeier and B. Piepenbreier, "Identification of steady-state inductances of PMSM using polynomial representations of the flux surfaces," in *Proc. IEEE 39th Annu. Conf. IEEE Ind. Electron. Soc.*, 2013, pp. 2899–2904.

[12] S. Kuehl, P. Landsmann, and R. M. Kennel, "Bivariate polynomial approximation of cross-saturated flux curves in synchronous machine models," in *Proc. IEEE Int. Energy Conf. Exhib.*, 2012, pp. 219–224.

[13] K. Liu, J. Feng, S. Guo, L. Xiao, and Z.-Q. Zhu, "Identification of flux linkage map of permanent magnet synchronous machines under uncertain circuit resistance and inverter nonlinearity," *IEEE Trans. Ind. Informat.*, vol. 14, no. 2, pp. 556–568, Feb. 2018.

[14] Z. Qu, T. Tuovinen, and M. Hinkkanen, "Inclusion of magnetic saturation in dynamic models of synchronous reluctance motors," in *Proc. IEEE 20th Int. Conf. Elect. Machines*, 2012, pp. 994–1000.

[15] M. Hinkkanen, P. Pescetto, E. Mölsä, S. E. Saarakkala, G. Pellegrino, and R. Bojoi, "Sensorless self-commissioning of synchronous reluctance motors at standstill without rotor locking," *IEEE Trans. Ind. Appl.*, vol. 53, no. 3, pp. 2120–2129, May/Jun. 2017.

[16] N. Bedetti, S. Calligaro, and R. Petrella, "Stand-still self-identification of flux characteristics for synchronous reluctance machines using novel saturation approximating function and multiple linear regression," *IEEE Trans. Ind. Appl.*, vol. 52, no. 4, pp. 3083–3092, Jul./Aug. 2016.

[17] A. Zanelli, J. Kullick, H. M. Eldeeb, G. Frison, C. M. Hackl, and M. Diehl, "Continuous control set nonlinear model predictive control of reluctance synchronous machines," *IEEE Trans. Control Syst. Technol.*, vol. 30, no. 1, pp. 130–141, Jan. 2022.

[18] L. Ortombina, F. Tinazzi, and M. Zigliotto, "Magnetic modeling of synchronous reluctance and internal permanent magnet motors using radial basis function networks," *IEEE Trans. Ind. Electron.*, vol. 65, no. 2, pp. 1140–1148, Feb. 2018.

[19] S.-W. Su, R. Kennel, and C. M. Hackl, "Analytical flux linkage approximation prototypes for reluctance synchronous machines," in *Proc. IEEE Int. Symp. Power Electron., Elect. Drives, Automat. Motion*, 2020, pp. 91–96.

[20] C. Hackl, *Non-Identifier Based Adaptive Control in Mechatronics*. Cham, Switzerland: Springer International Publishing, 2017.

[21] J. A. Melkebeek and J. L. Willems, "Reciprocity relations for the mutual inductances between orthogonal axis windings in saturated salient-pole machines," *IEEE Trans. Ind. Appl.*, vol. 26, no. 1, pp. 107–114, Jan./Feb. 1990.

[22] H. Gavin, "The levenberg-marquardt method for nonlinear least squares curve-fitting problems," *Dep. Civil Environ. Eng., Duke Univ.*, vol. 28, pp. 1–5, 2011.

[23] E. Armando, P. Guglielmi, G. Pellegrino, M. Pastorelli, and A. Vagati, "Accurate modeling and performance analysis of IPM-PMASR motors," *IEEE Trans. Ind. Appl.*, vol. 45, no. 1, pp. 123–130, Jan./Feb. 2009.

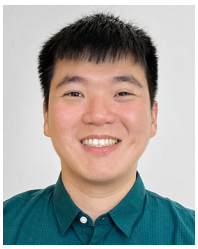

SHIH-WEI SU was born in 1993 in Taichung, Taiwan. He received the B.Sc. degree in electrical engineering from the National Taipei University of Technology, Taipei, Taiwan, in 2015, and the M.Sc. degree in electrical engineering from National Tsing Hua University, Hsinchu, Taiwan, in 2017. He is currently working toward the Ph.D. degree with the Chair of Electrical Drive Systems and Power Electronics, Technical University of Munich, Munich, Germany. His research interests include power electronics, electrical drives, modeling of electrical machines and encoderless control.

CHRISTOPH M. HACKL (Senior Member, IEEE) was born in 1977 in Mannheim, Germany. After studying electrical engineering (with focus on mechatronics and systems and control) from the Technical University of Munich (TUM), Germany and University of Wisconsin-Madison, Madison, WI, USA, he received the B.Sc., Dipl.-Ing., and Dr.-Ing. (Ph.D.) degrees in electrical engineering in 2003, 2004 and 2012, respectively, from TUM. Since 2004, he has been teaching electrical drives, power electronics, and mechatronic and renewable energy systems. Since 2014, he has been the Head of the Research Group Control of Renewable Energy Systems (CRES) with TUM. In 2018, he became a Professor for Electrical Machines and Drives and the Head of the Laboratory for Mechatronic and Renewable Energy Systems (LMRES) with the Hochschule München (HM) University of Applied Sciences, Munich, Germany. In 2019, he completed his habilitation on Mechatronic and Renewable Energy Systems and co-founded the research Institute for Sustainable Energy Systems (ISES), HM, which he co-heads since then. His research interests include nonlinear, adaptive and optimal control and design of electrical drives, and mechatronic and renewable energy systems.

RALPH KENNEL (Senior Member, IEEE) was born in Kaiserslautern, Germany, in 1955. He received the Diploma and Dr. Ing. (Ph.D.) degrees in electrical engineering from the University of Kaiserslautern, Kaiserslautern, Germany, in 1979 and 1984, respectively.

From 1983 to 1999, he worked on several positions with Robert BOSCH GmbH (Germany). Until 1997, he was responsible for the development of servo drives. From 1994 to 1999, he was a Visiting Professor with the University of Newcastle-upon-Tyne, Newcastle-upon-Tyne, U.K. From 1999 to 2008, he was a Professor of Electrical Machines and Drives with Wuppertal University, Wuppertal, Germany. Since 2008, he has been a Professor of Electrical Drive Systems and Power Electronics with Technical University of Munich, Munich, Germany. His main research interests include renewable energy systems, sensorless control of ac drives, predictive control of power electronics, and hardware-in-the-loop systems. Dr. Kennel is a Chartered Engineer in the U.K. within IEEE, he is a Treasurer of the Germany Section and also ECCE Global Partnership Chair of the Power Electronics society. He is an Associate Editor for the IEEE TRANSACTIONS ON POWER ELECTRONICS.